What drives deformation?

Most simply put, it is when stresses overcome strength

So, what is strength? Where do stresses come from?

Compression, strain rate 10^{-15} s^{-1}, quartzite over olivene

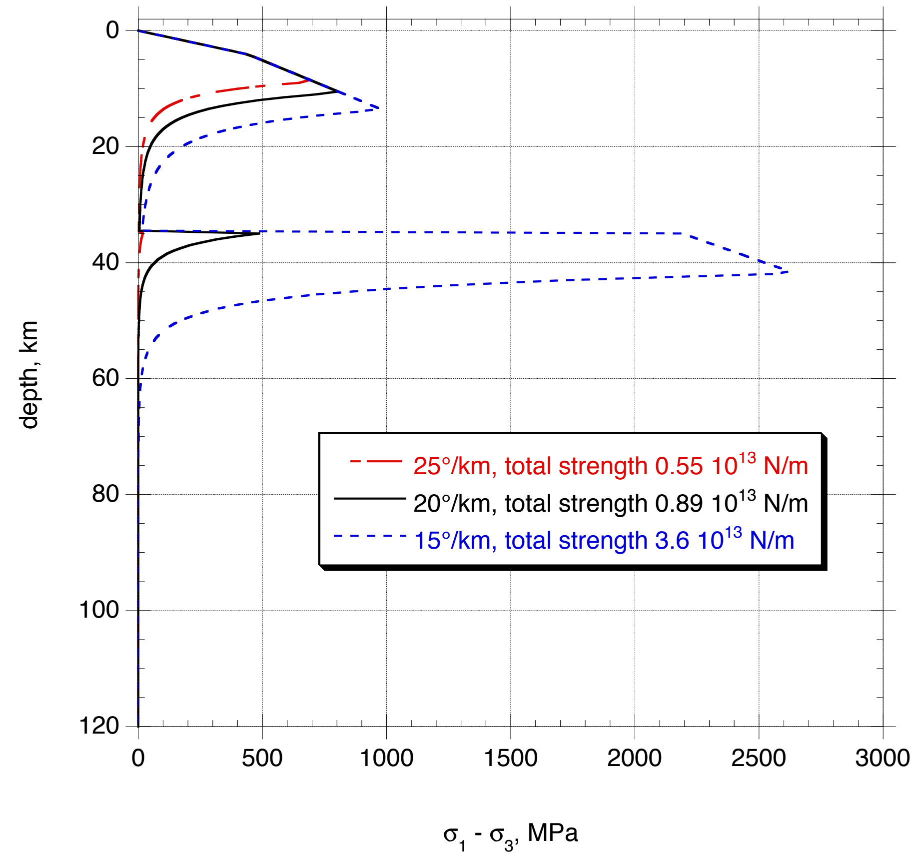

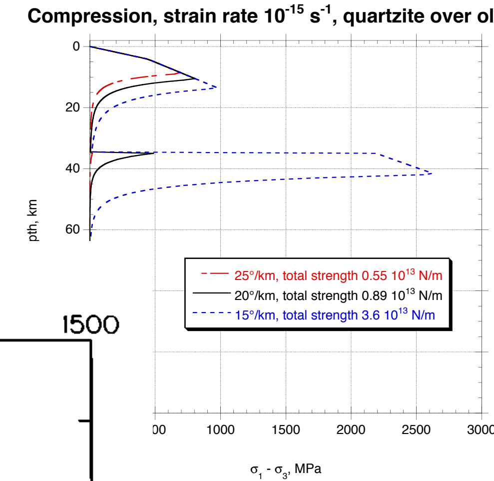

Overall strength much lower in extension

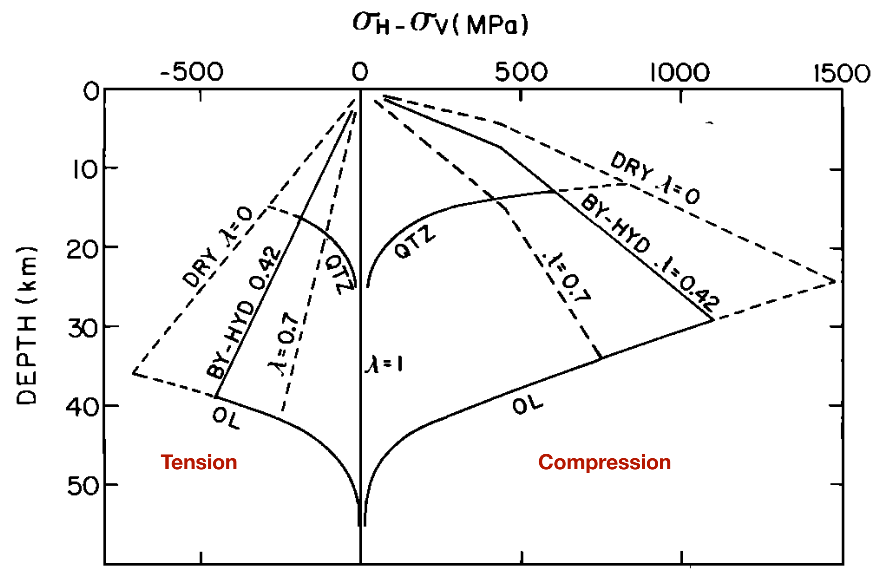

Fig. 5. Difference between maximum or minimum horizontal stress and the vertical stress as a function of depth. Values of λ give pore pressure level. See also Figure 4.

What of stresses?

For edge forces, deformation should decrease with distance from edge…

ε_{xx} (proportional to σ_{xx})

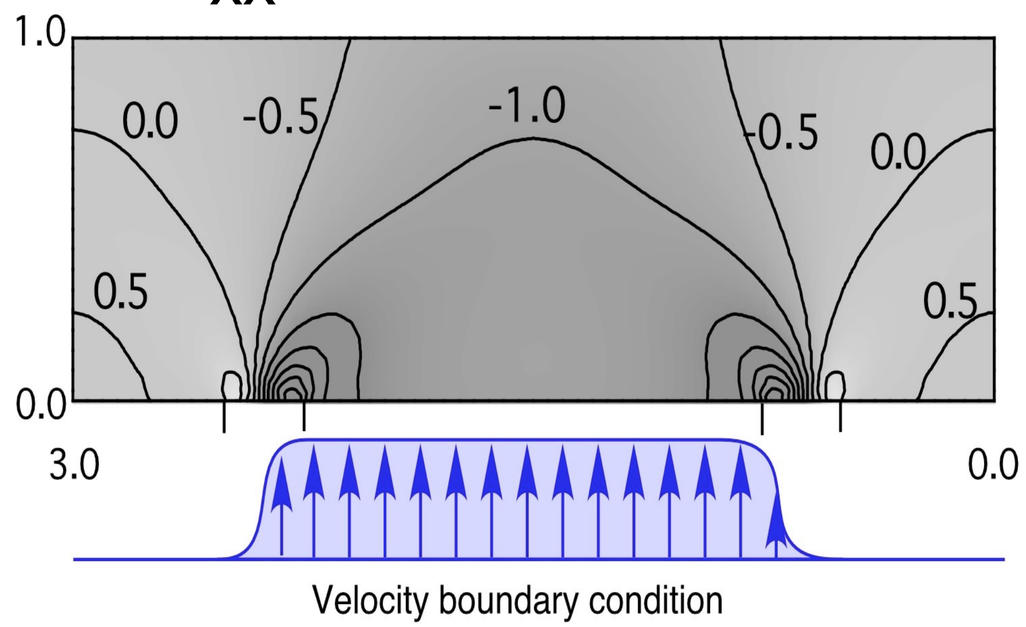

Modified from Sonder and Jones (1999)

Basal shear stress

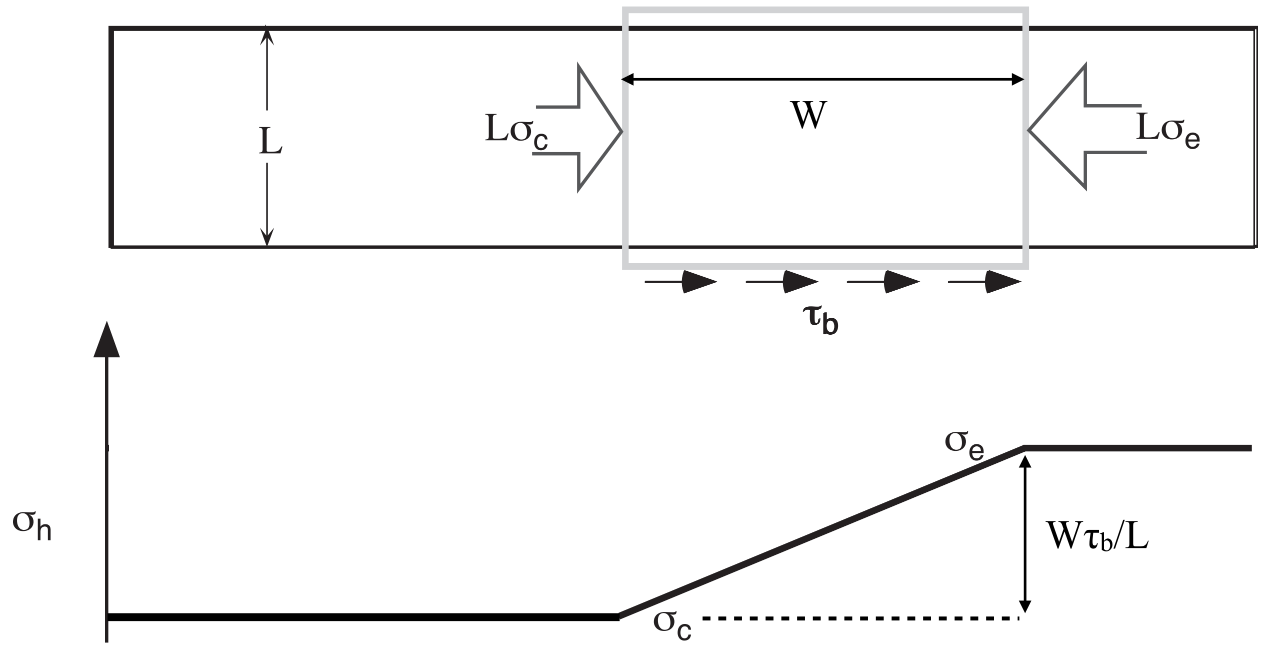

…great way to get higher horizontal stresses far inland (produces shortening to the right)

But for normal faulting, can we get lower stresses?

This is the classic flat slab model for the Laramide; note it requires that basal shear to be pretty high.

Basal shear

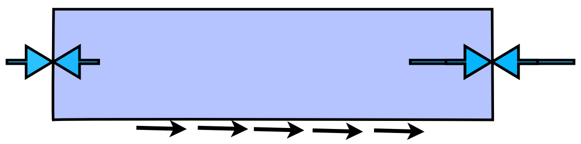

Basal shear increases horizontal normal stresses in direction of shear

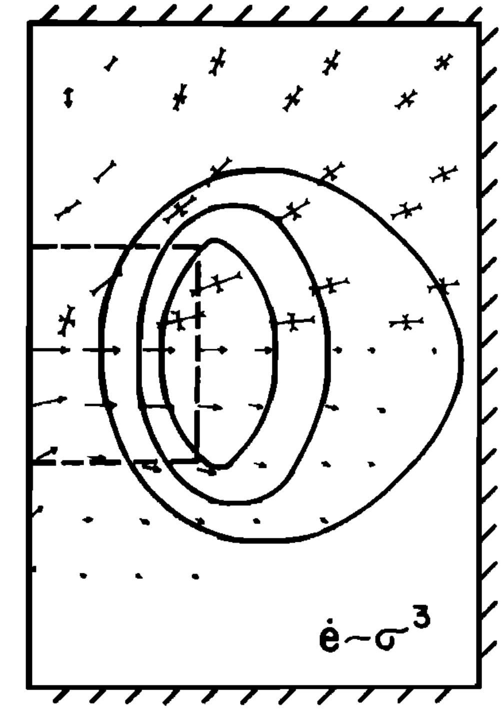

Bird, *Tectonics*, 1984

Contours are rate of crustal thickening (not relevant here), stresses in top, velocities at bottom.

Basal shear stress

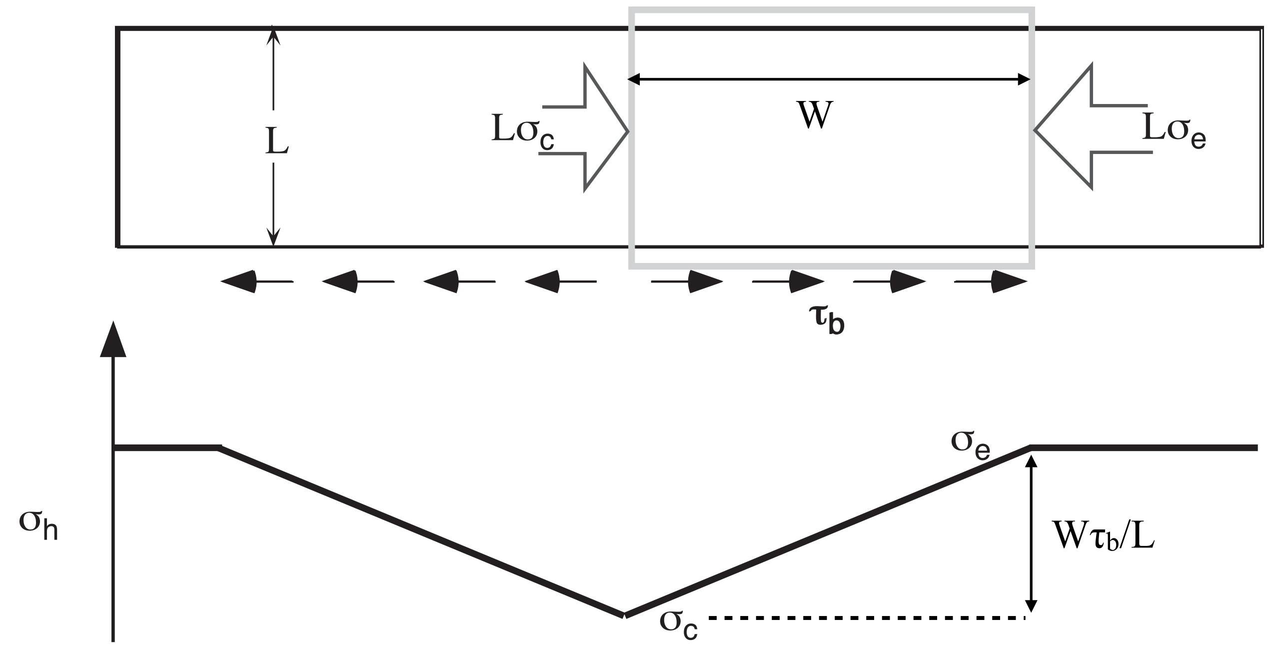

Diverging basal shears can produce low horizontal stress but tends to be tightly focused

This might not be such a terrible model for some back-arc situations, but not so wonderful for extension in continents in general.

Gravitational Potential Energy and stresses

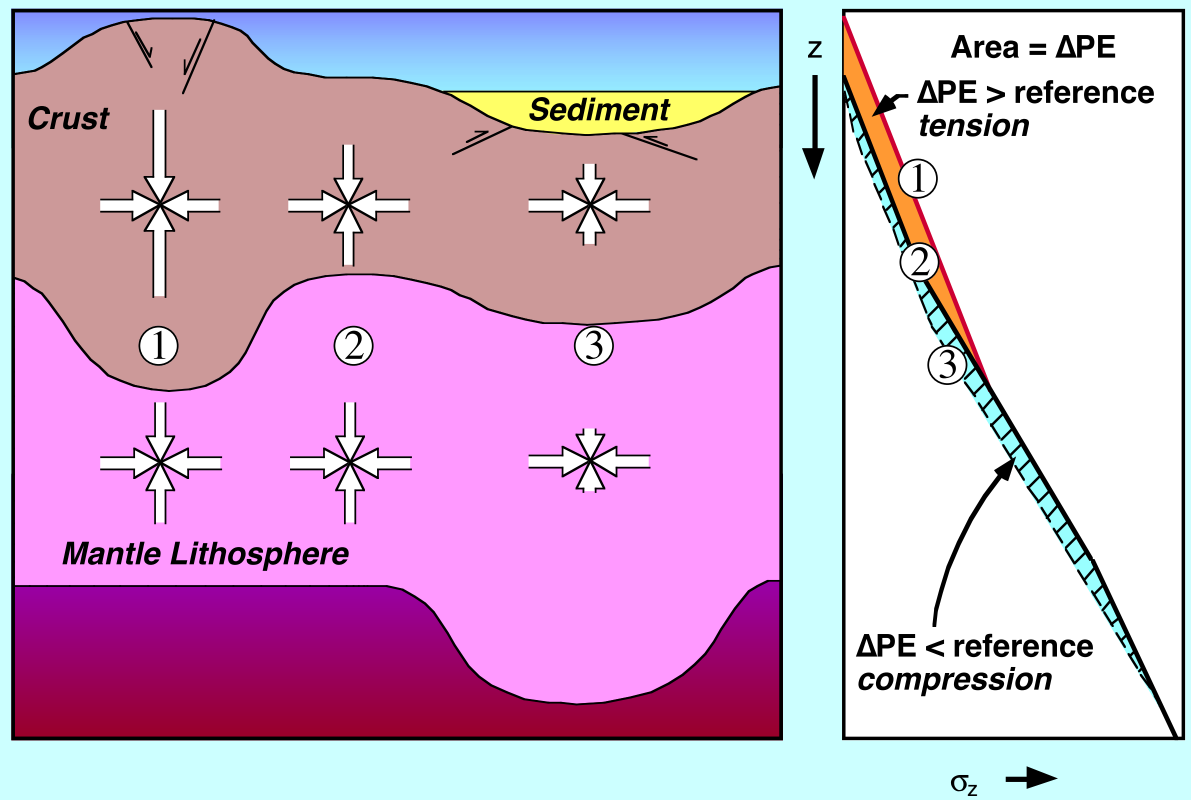

Body forces

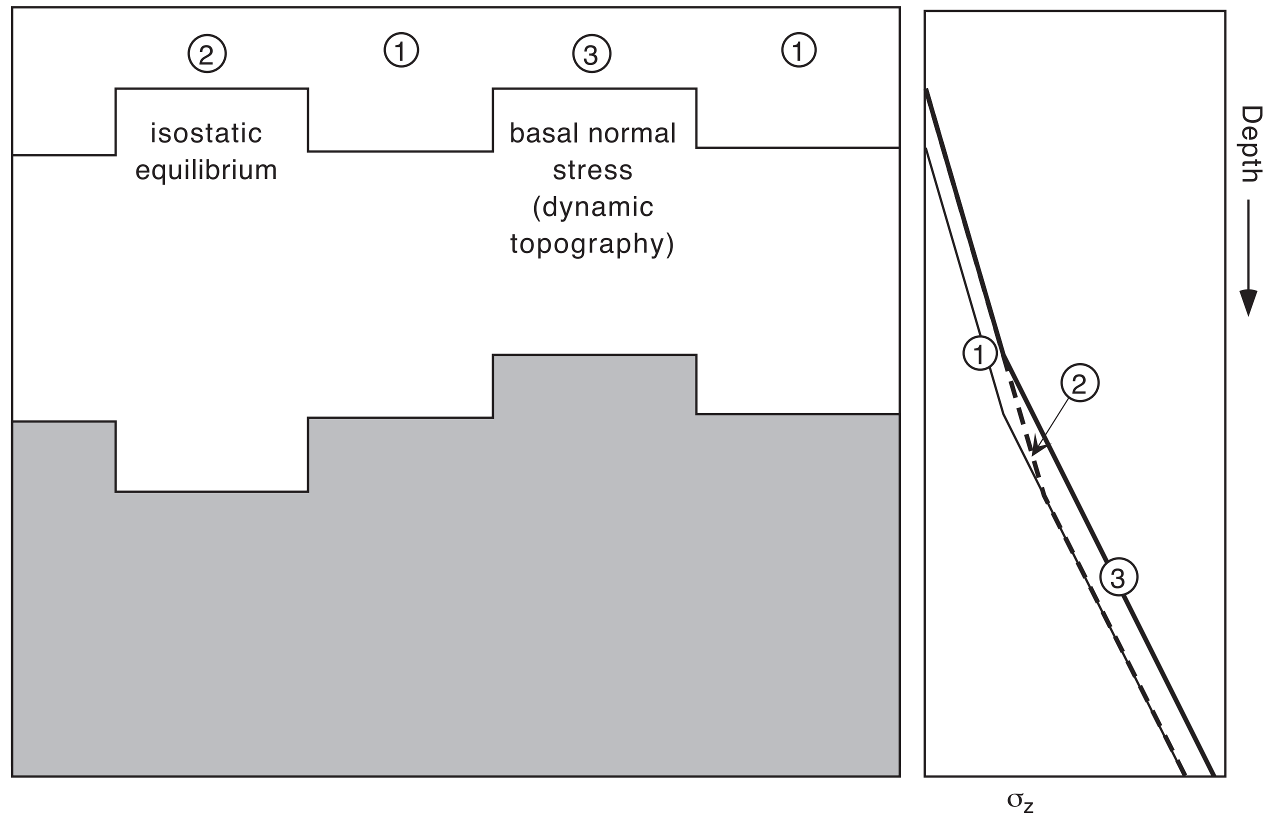

Column 1 is an isotropic stress state (no deformation no matter how weak it is).

$$\mathrm{GPE} = \int_{0}^{z_c+\varepsilon} \rho(z') g z' \, dz'$$

$$= -\int_{z_c}^{-\varepsilon} \rho(z) g (z_c - z) \, dz$$

$$= g z_c \int_{-\varepsilon}^{z_c} \rho(z) dz - \int_{-\varepsilon}^{z_c} \rho(z) g z dz$$

Isostasy

$$\mathrm{GPE} = g z_c \int_{-\varepsilon}^{z_c} \rho(z)\,dz - \int_{-\varepsilon}^{z_c} \rho(z)\, g z\, dz$$

$$\Delta\mathrm{GPE} = \int_{H_0}^{z_c} \rho_a g z\, dz - \int_{-\varepsilon}^{z_c} \rho(z)\, g z\, dz$$

Asthenosphere

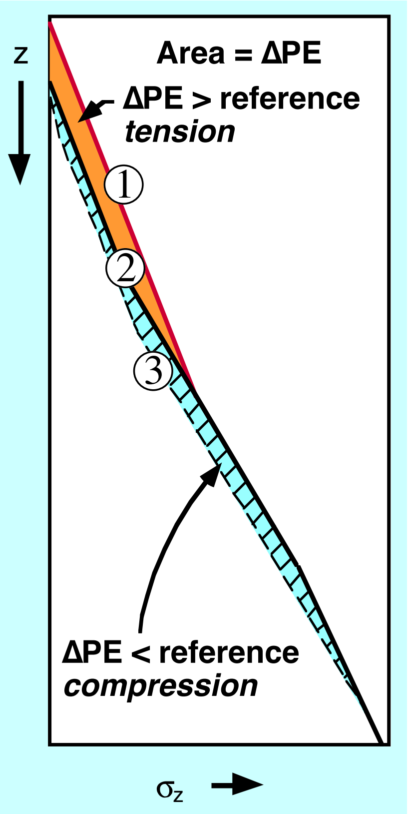

Could make point that GPE is proportional to strain rate for Newtonian viscosity

$$\int_{-\varepsilon}^{z_c} \sigma_z(z)\,dz = \int_{-\varepsilon}^{z_c}\int_{-\varepsilon}^{z} g\rho(z')\,dz'dz$$

$$= \left[zg\int \rho\, dz'\right]_{-\varepsilon}^{z_c} - \int_{-\varepsilon}^{z_c} gz\rho(z)\,dz$$

$$= \left[z\sigma_z\right]_{-\varepsilon}^{z_c} - \int_{-\varepsilon}^{z_c} gz\rho(z)\,dz$$

$$= z_c\int_{-\varepsilon}^{z_c} g\rho(z)\,dz - \int_{-\varepsilon}^{z_c} gz\rho(z)\,dz = GPE$$

$$\frac{\partial \bar{\tau}_{ij}}{\partial x_j} + \frac{\partial \bar{\tau}_{zz}}{\partial x_i} = \frac{1}{L}\frac{\partial (PE)}{\partial x_i}$$

Can make stresses by changing structure of the lithosphere

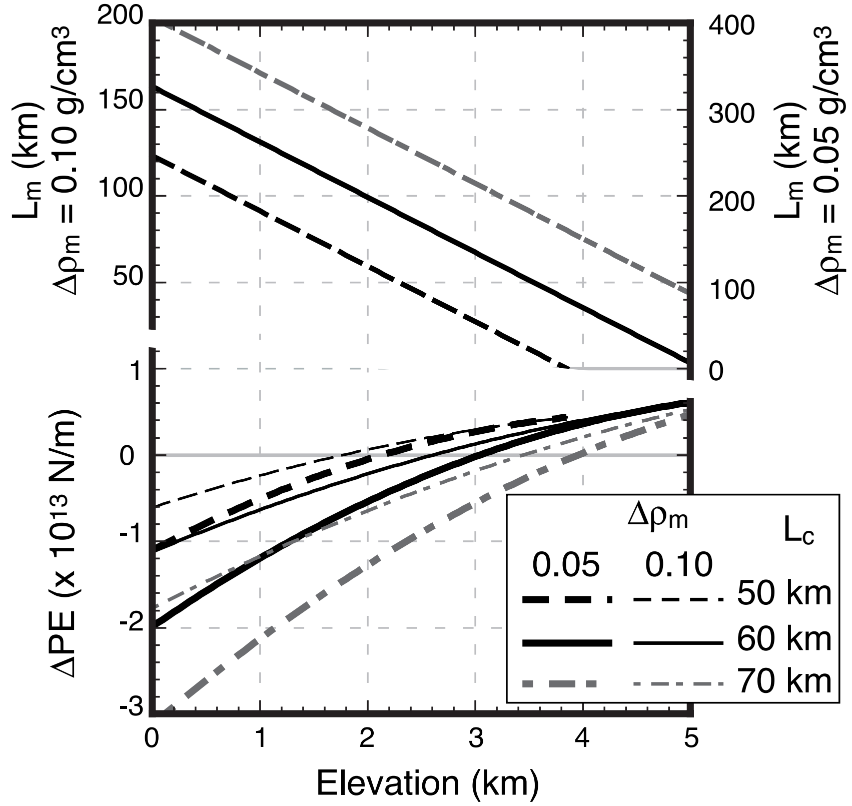

Figure 3. ΔPE for lithospheric columns with different crustal thicknesses (*L_c*) as a function of elevation. Two mean density contrasts ($\Delta\rho_m$) between mantle lithosphere and asthenosphere are illustrated. Note that low elevations with 50–70-km-thick crust likely for the early Tertiary Great Basin would require very thick or exceptionally dense mantle lithosphere and imply very negative values of ΔPE.

Jones et al., *Geology*, 1998

Relation of crustal thickness, elevation, and GPE.

Figure 2. Evolution of orogen with initial phase of uniform lithospheric thickening (dashed lines) followed by thinning of mantle lithosphere once the orogen reaches elevations of 2, 3, or 4 km (solid lines). Note that elevation always increases, but ΔPE reverses once mantle lithosphere begins to be removed. Gray lines indicate conditions under which extension is possible. Crustal thickness L_c = 30 km at outset; L_m = 86 km; ρ_c = 2.8 g/cm^3. An equivalent path in Figure 1 would proceed toward the right from thickening factor = 1 on the solid line, then up toward the dashed curve once thinning of the mantle lithosphere begins.

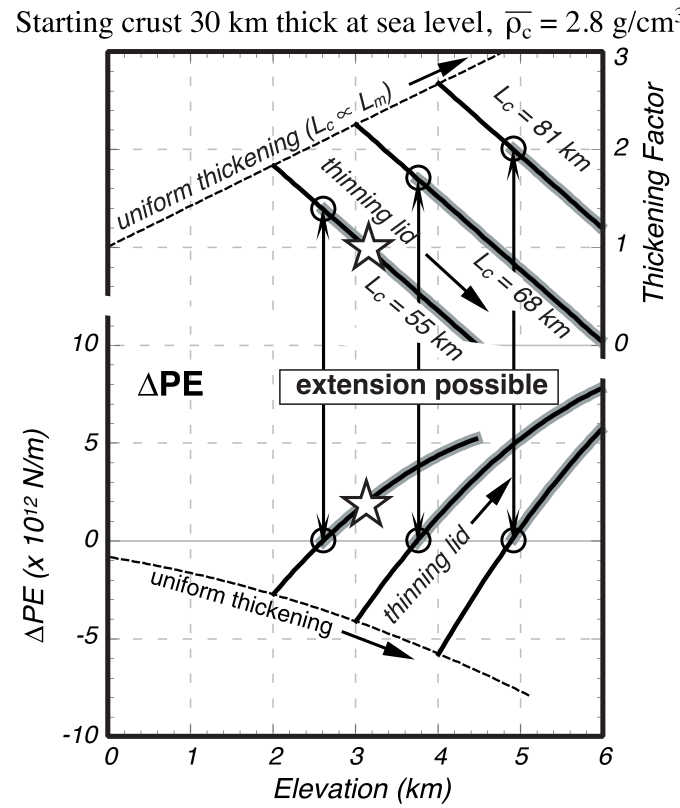

Jones et al., *Geology*, 1998

This is set up to move into paleoelevation studies.

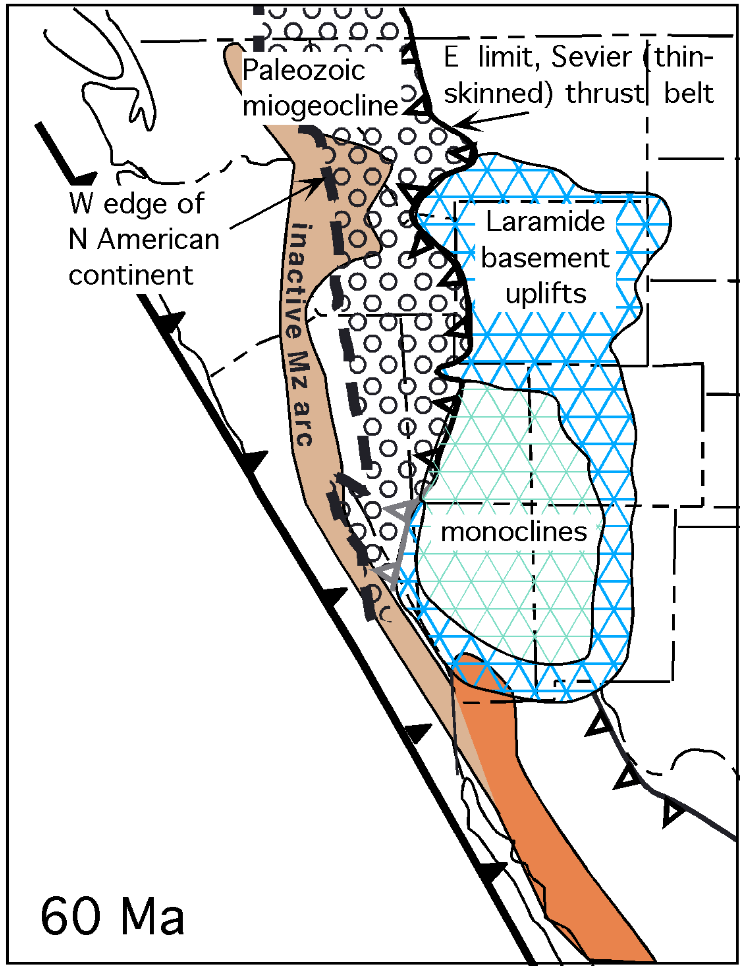

Sonder & Jones, *Ann. Rev Earth Plan. Sci*, 1999

When we look at this at the broadest scales, do we see the causes of extension? Is it strength? Is it stress?

Dark orange is calc-alkaline volcanic areas (some interpret as arc)

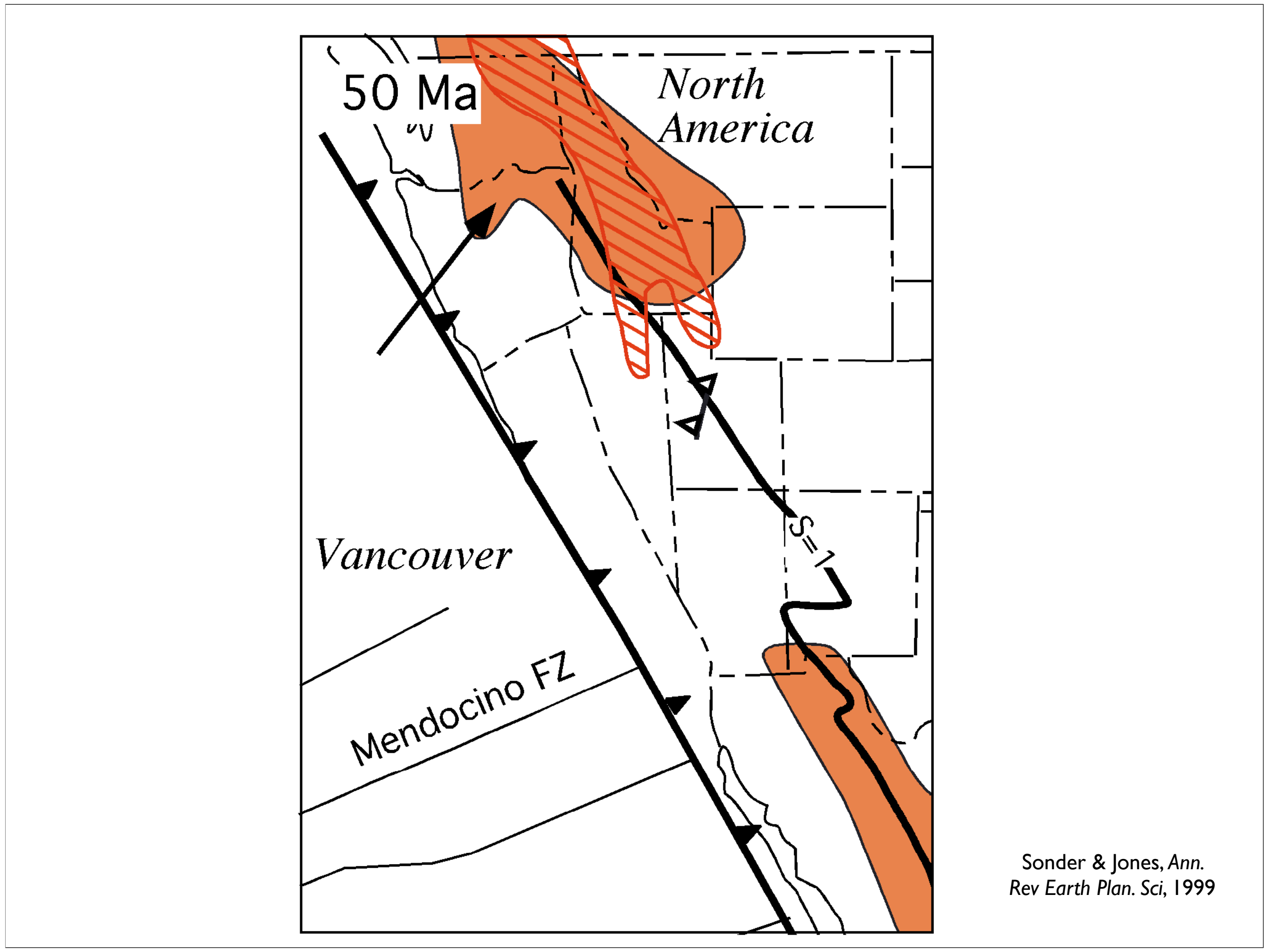

Big arrow is relative plate motion. Large heavy line (S=1) indicates position along which slab has fairly constant thermal state. “At each point on the slab, S equals the time since subduction divided by one-tenth of the age of that point at the time it was subducted.”
S=1 is approximately maximum depth of seismic slab. S = 10T/(A-T-C) where T is time since subduction, A age of magnetic anomaly and C is time of map construction (so A-C is age of slab at subduction.

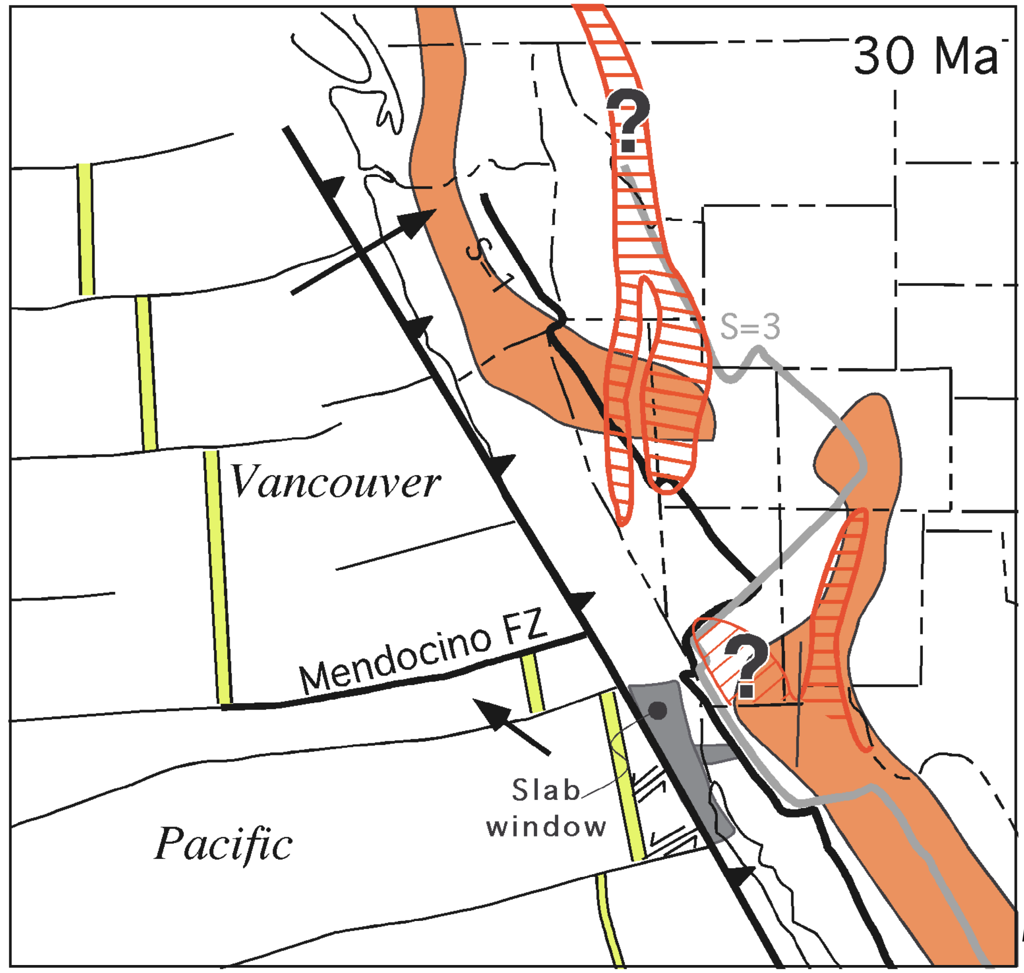

Sonder & Jones, *Ann. Rev Earth Plan. Sci*, 1999

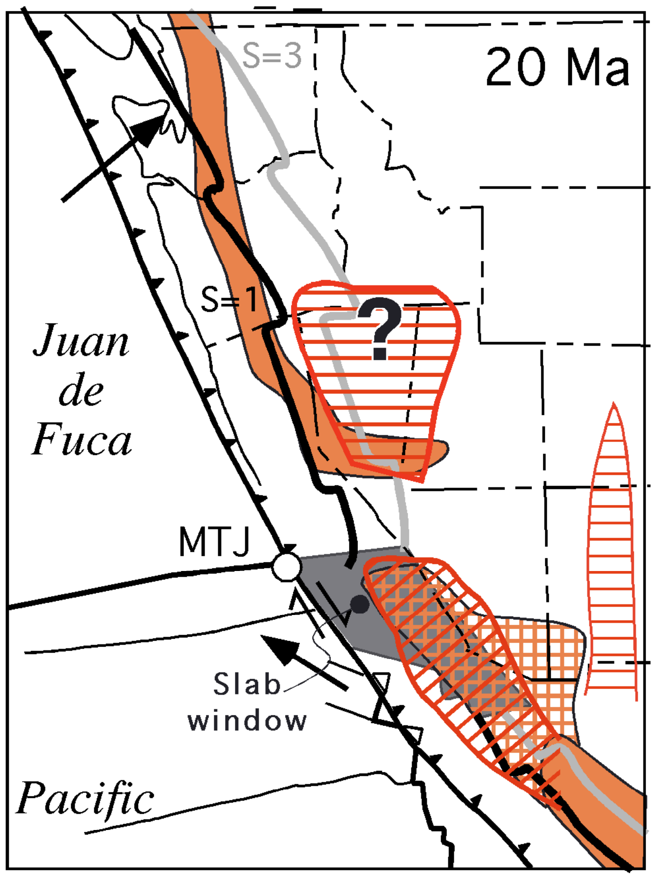

Sonder & Jones, *Ann. Rev Earth Plan. Sci*, 1999

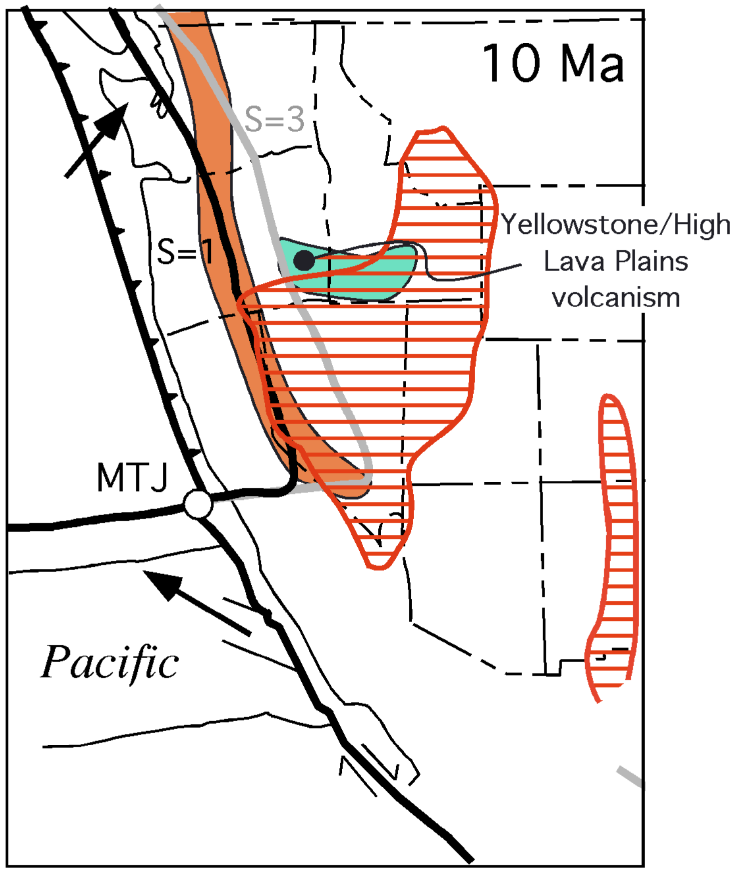

Sonder & Jones, *Ann. Rev Earth Plan. Sci*, 1999

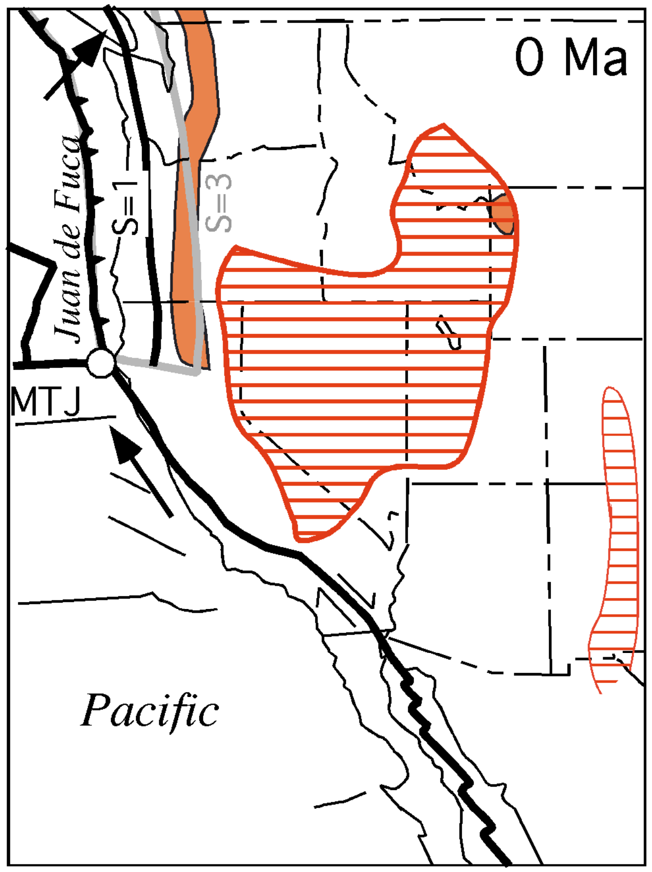

Sonder & Jones, *Ann. Rev Earth Plan. Sci*, 1999

Note that the B&R extent seems unrelated to the triple junction.

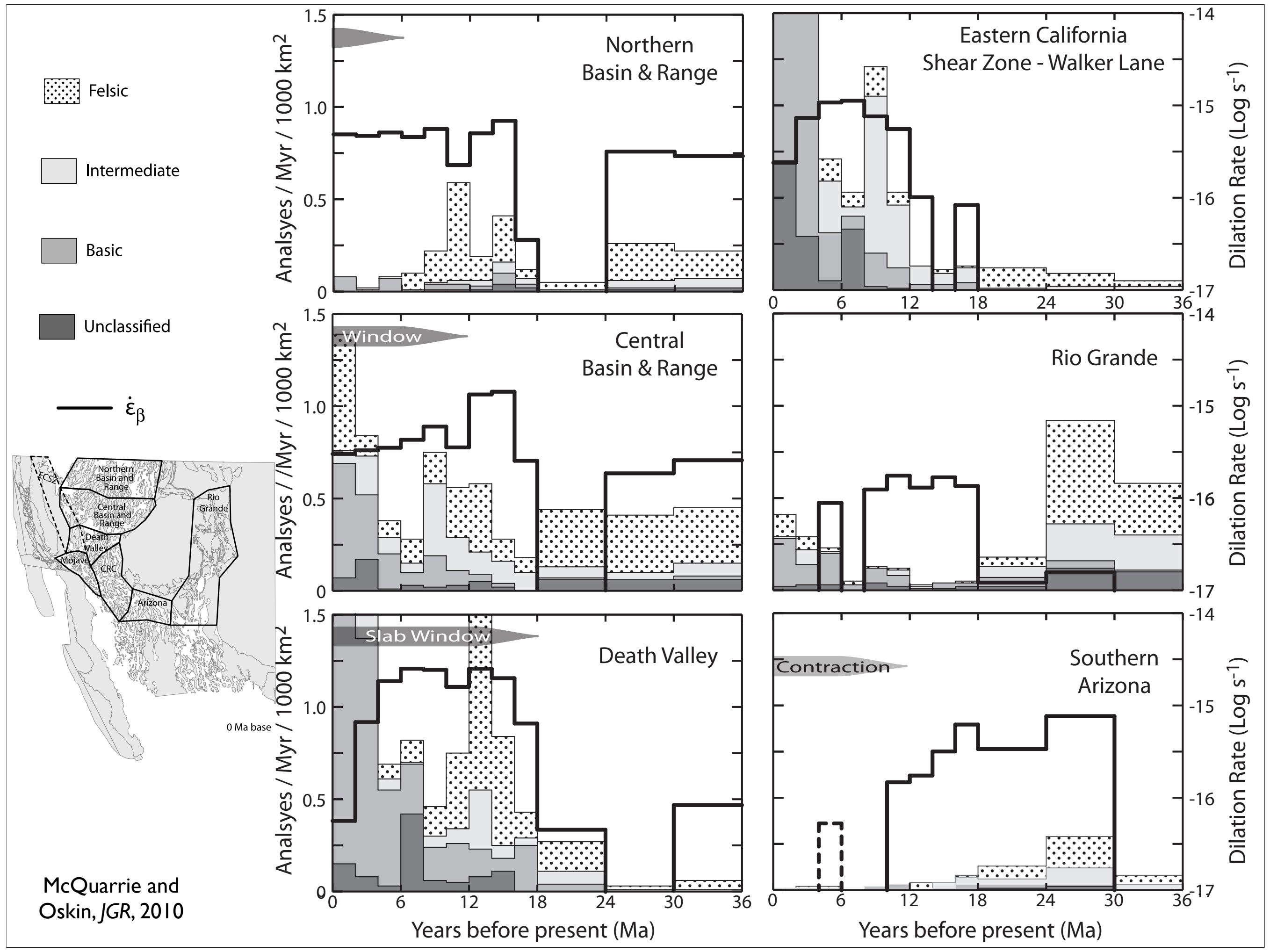
Felsic
Intermediate
Basic
Unclassified
$\dot{\varepsilon}_\beta$
Northern Basin and Range
Central Basin and Range
Rio Grande
Death Valley
Mojave
CRC
Arizona
0 Ma base
McQuarrie and Oskin, *JGR*, 2010
Northern Basin & Range
Eastern California Shear Zone - Walker Lane
Central Basin & Range
Window
Rio Grande
Slab Window
Death Valley
Contraction
Southern Arizona
Analsyes / Myr / 1000 km^2
Dilation Rate (Log s^{-1})
Years before present (Ma)

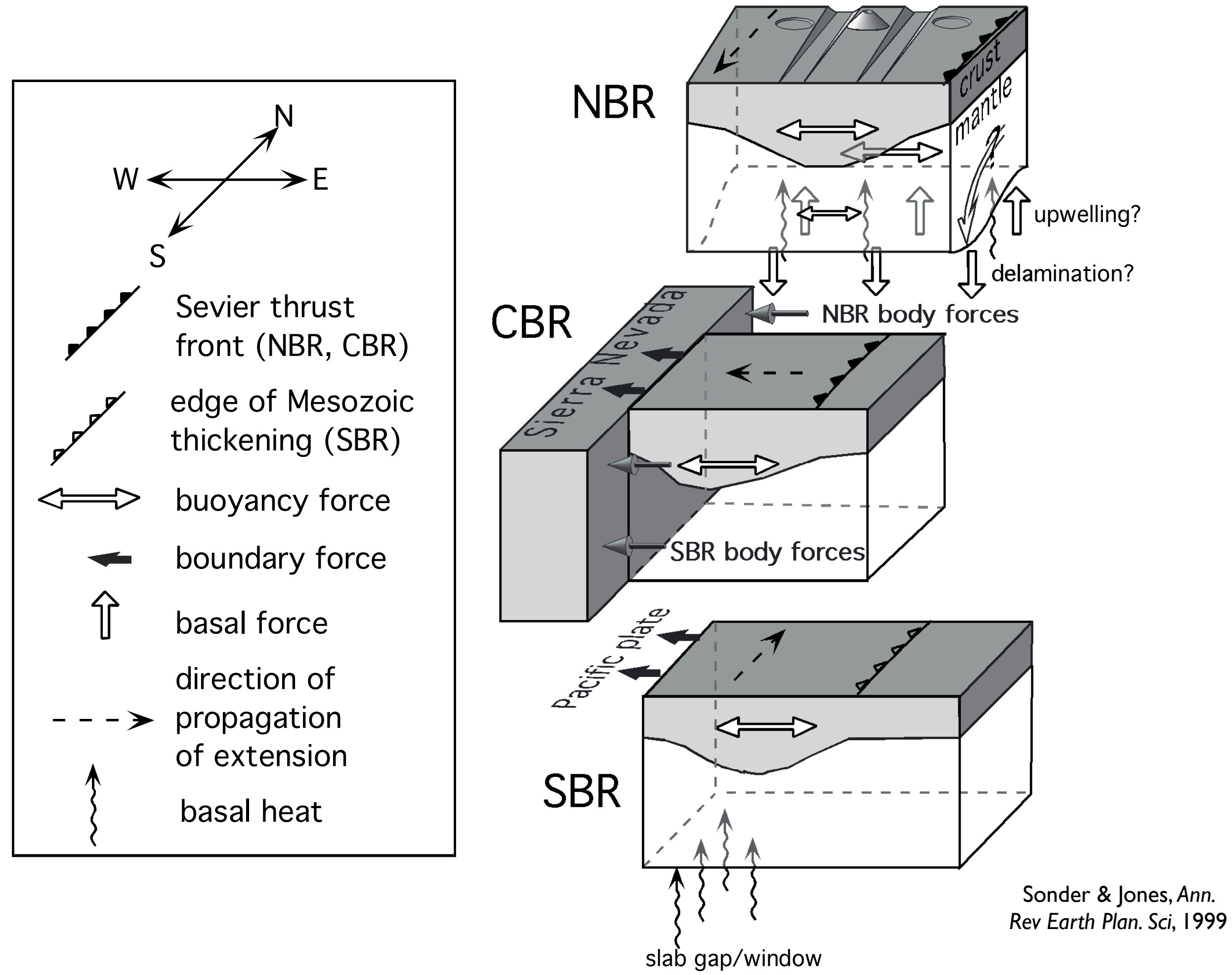

Sonder & Jones, *Ann. Rev Earth Plan. Sci*, 1999

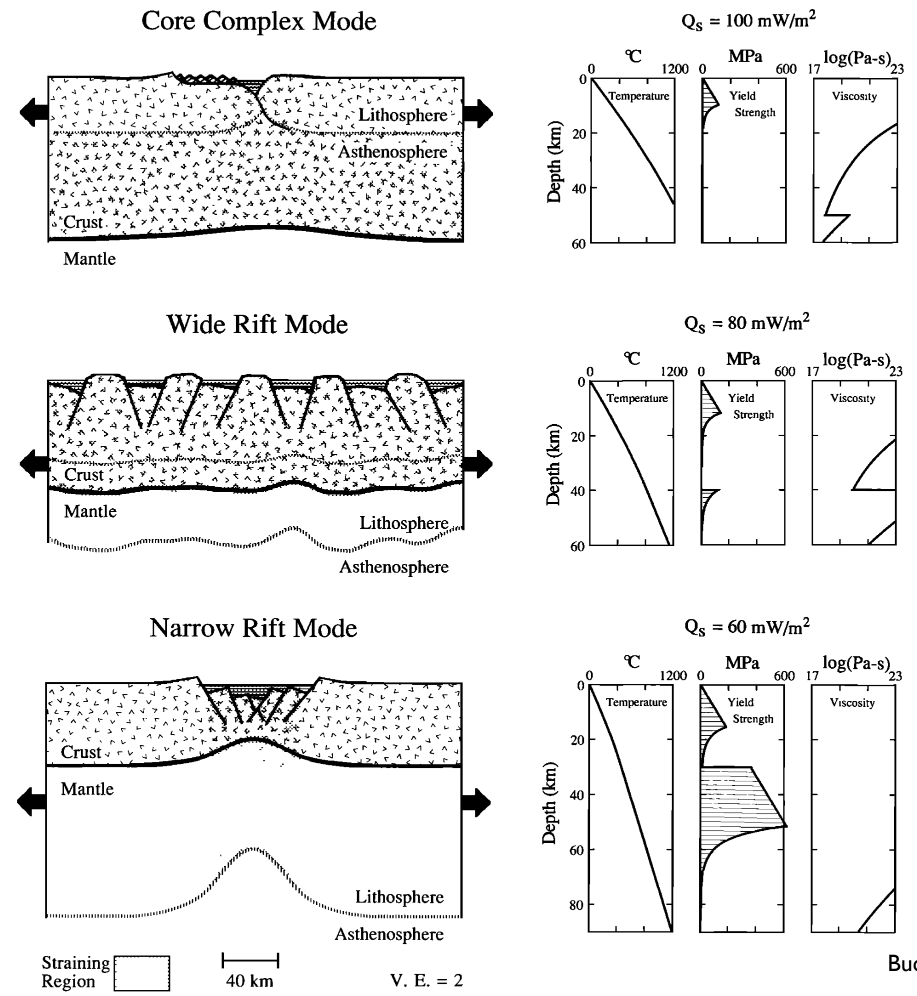

Buck, *JGR*, 1991

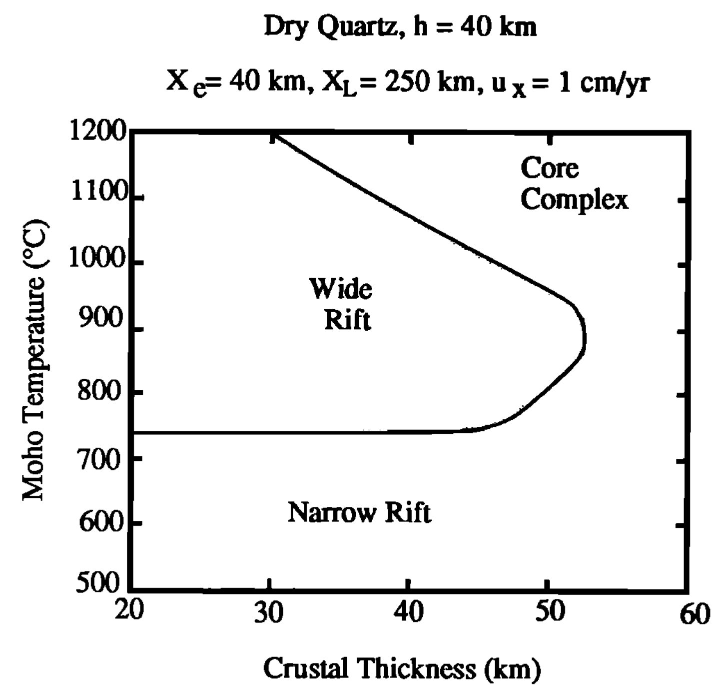

Buck, *JGR*, 1991

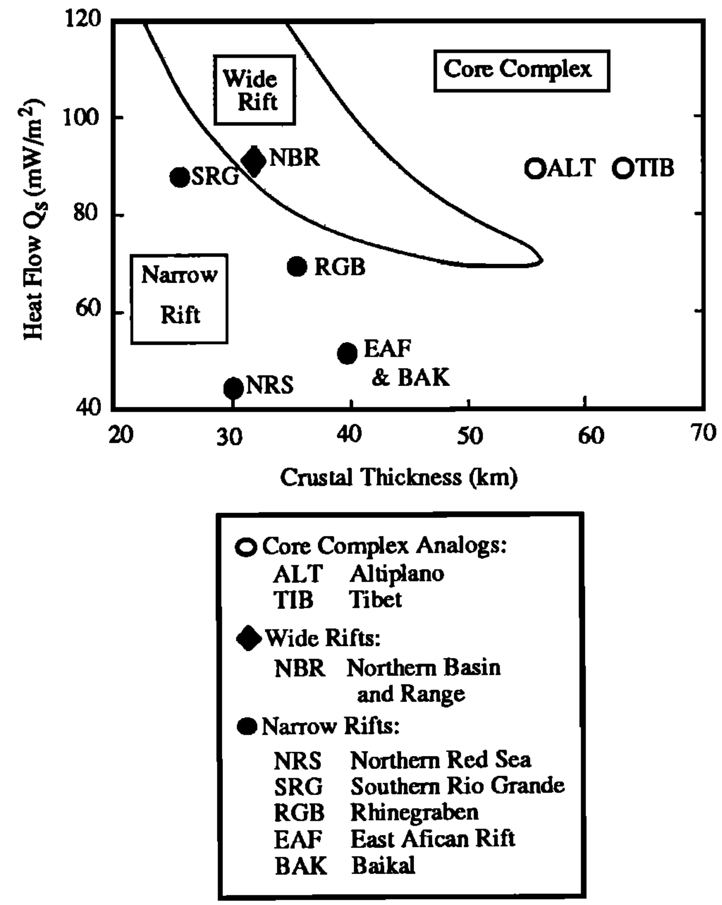

Buck, *JGR*, 1991

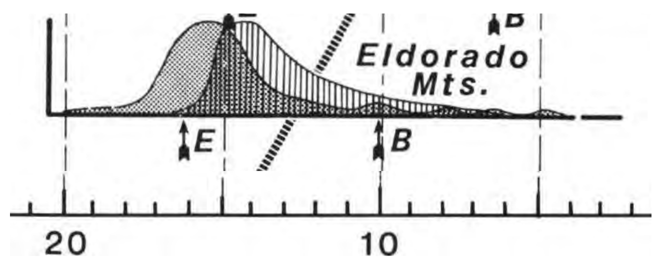

Gans et al., *GSA Spec. Paper*, *233*, 1989

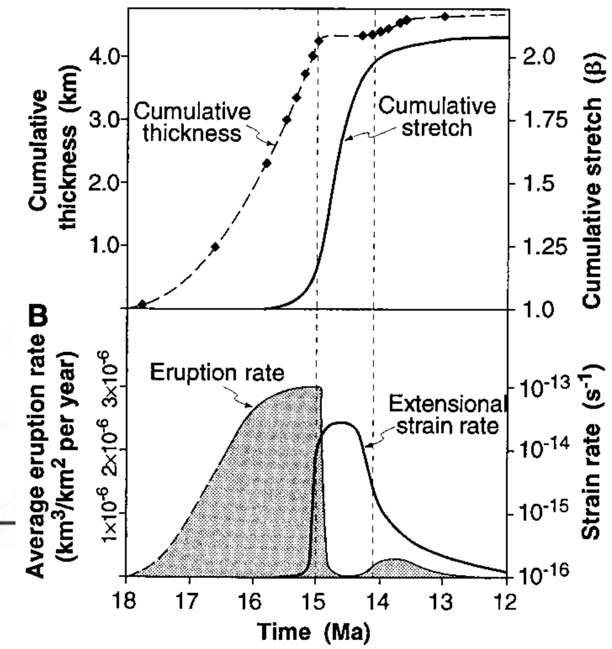

Gans and Bohrson, *Science*, 1997

Closer examination of at least one complex suggests that while tightly related in time, faulting and volcanism are not coeval.

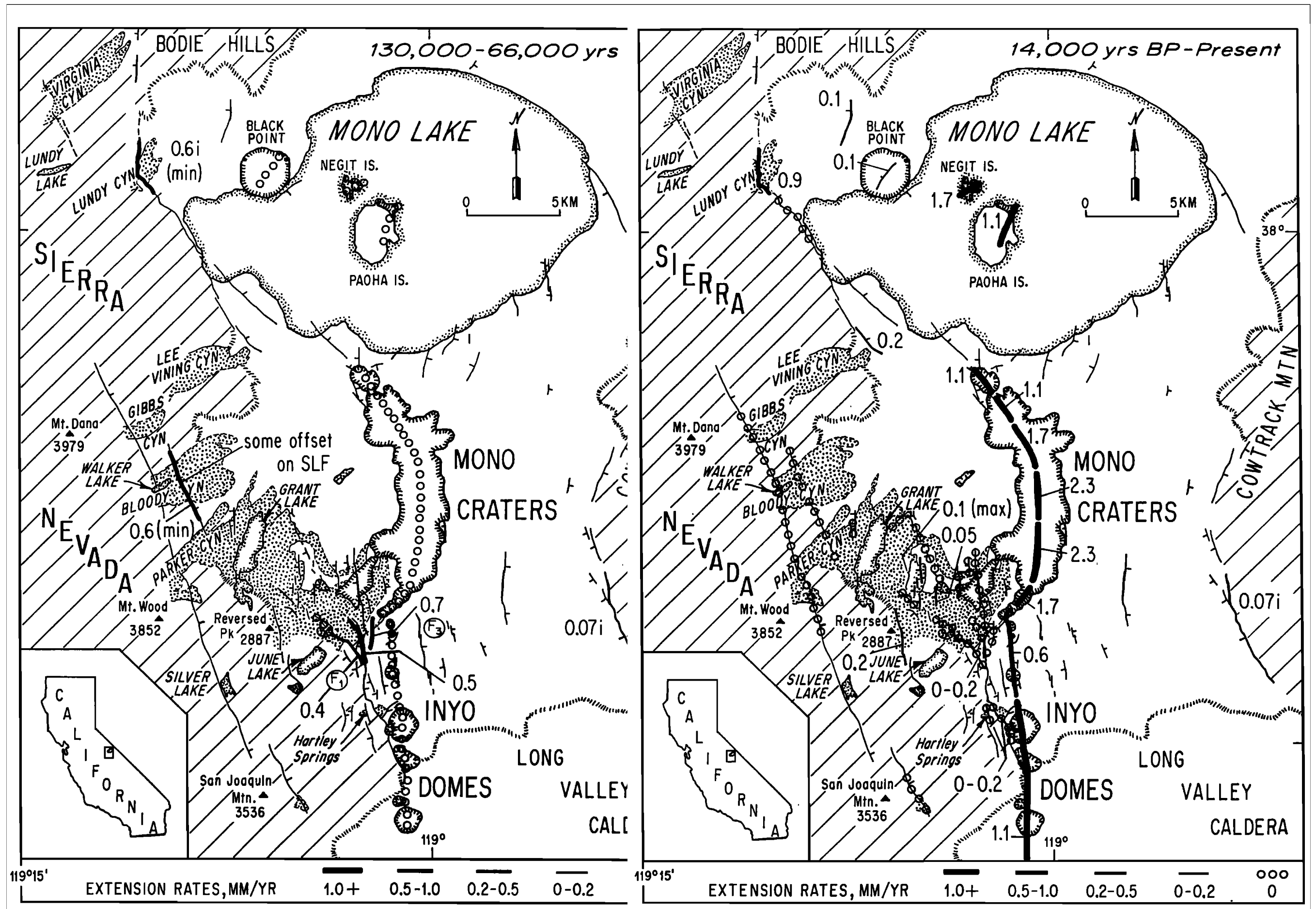

Bursik and Sieh, *JGR*, 1989

Initiation of volcanism has shifted extension into diking--so volcanism could represent extension.

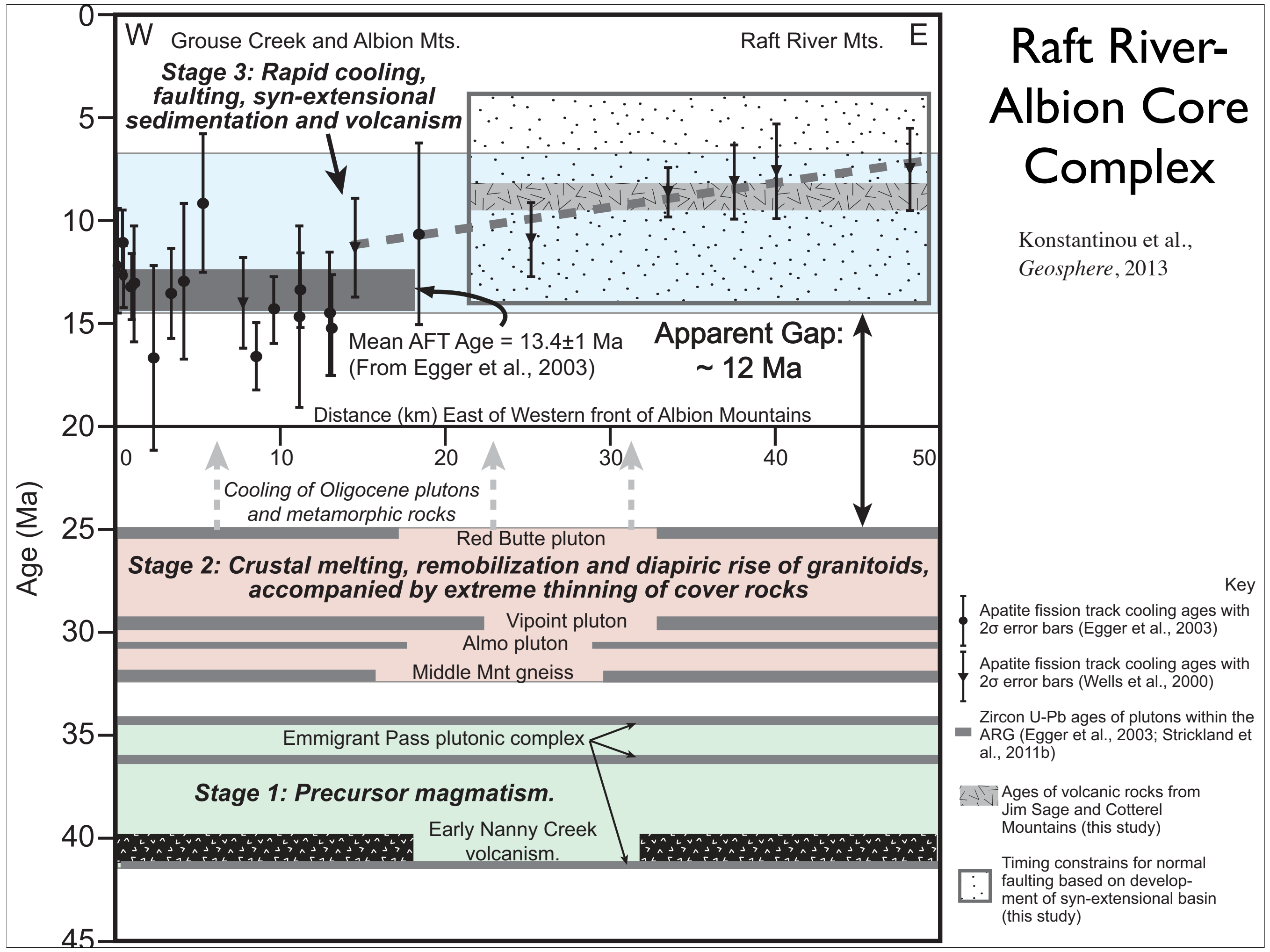

Or, maybe, we have grossly overestimated extension in Paleogene.

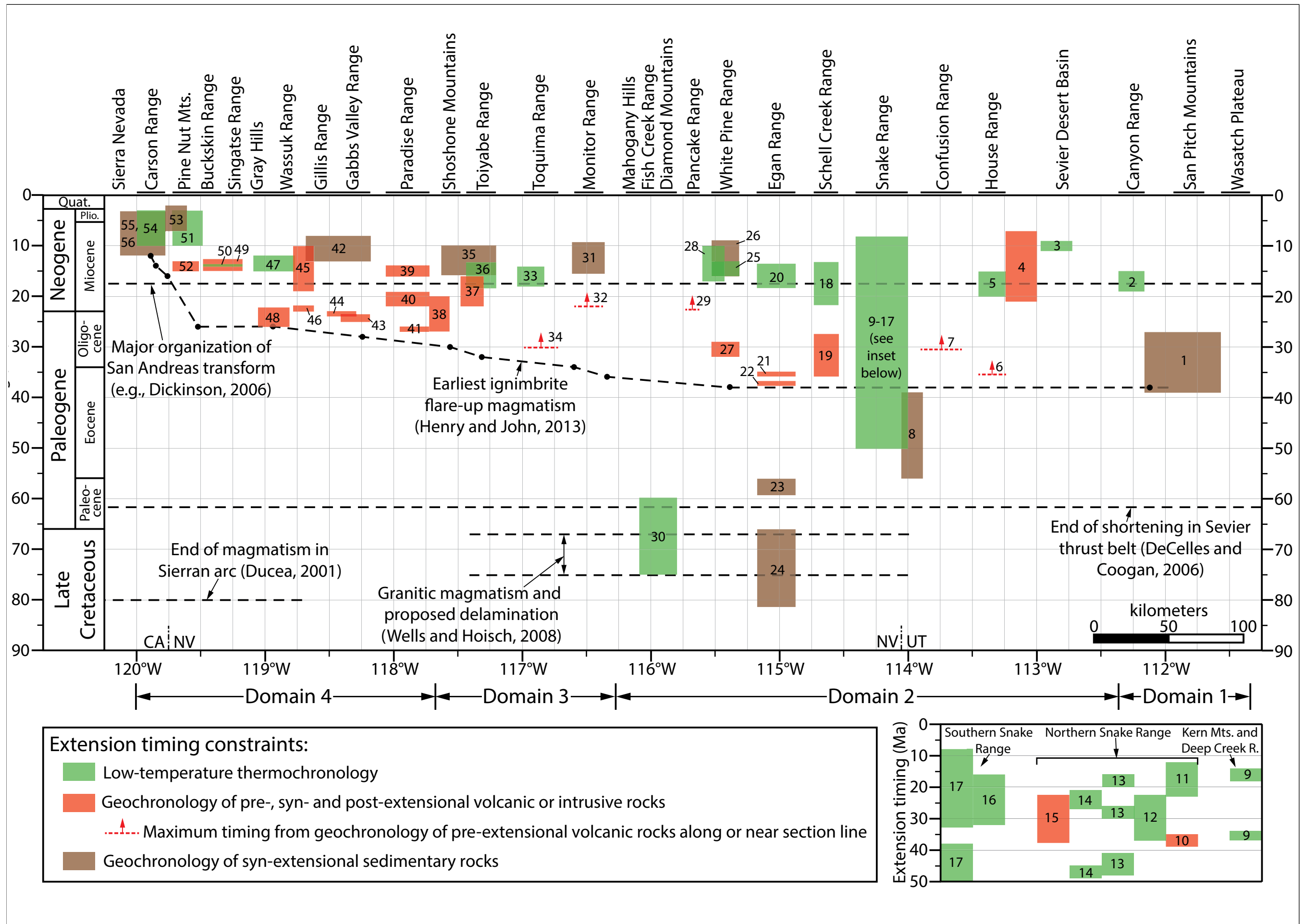

Long, *GSA Bull,* 2019

Profile across northern NV–UT…not a simple, clean story here. But you do see the c 17 Ma appearance of more widespread extension (but labeling that SAF appearance is misleading; at this latitude transform boundary only started c 5 Ma).

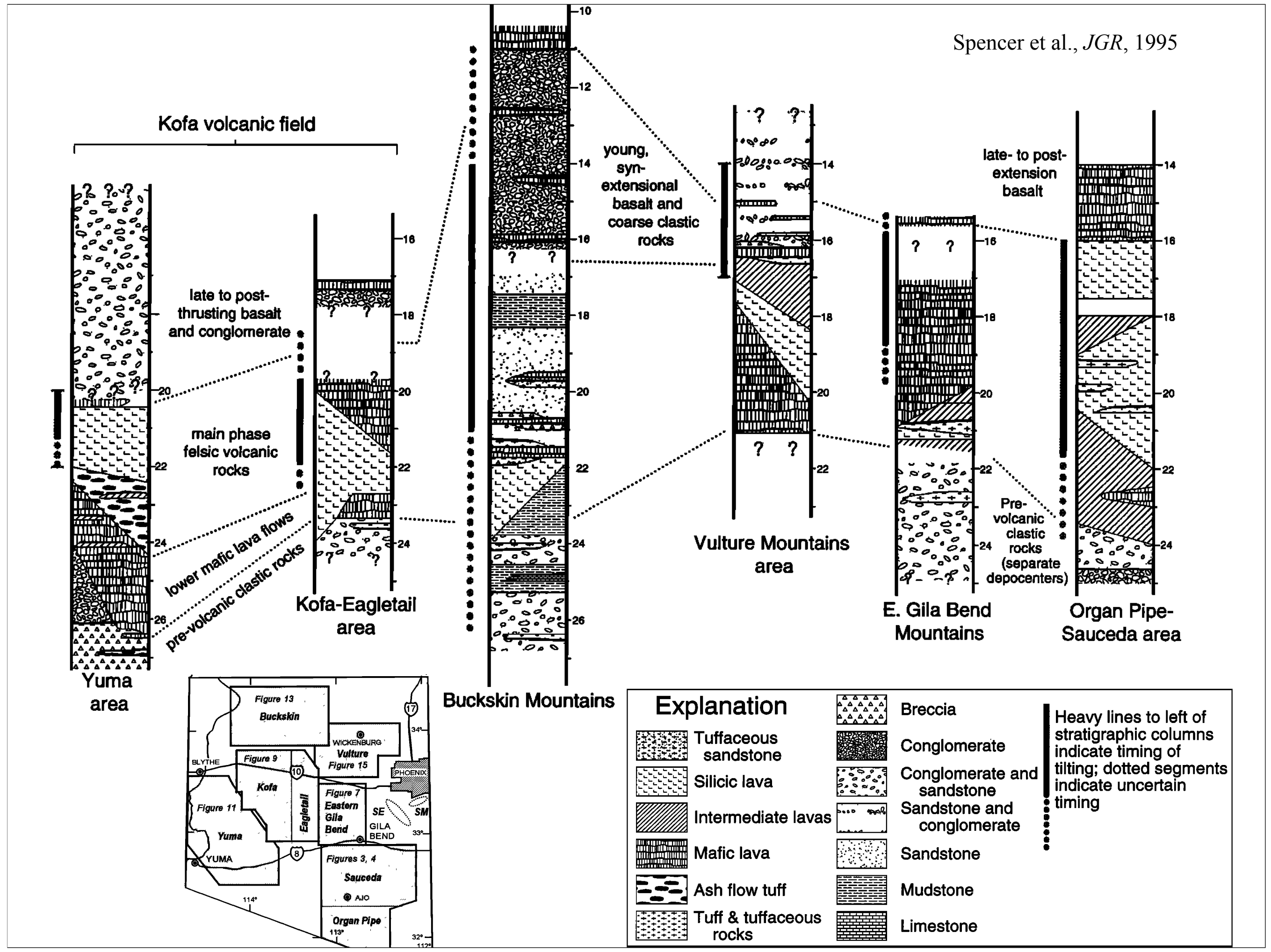

Arizona relation of tilting to volcanism. Note too some thick clastic sequences preceding volcanism.

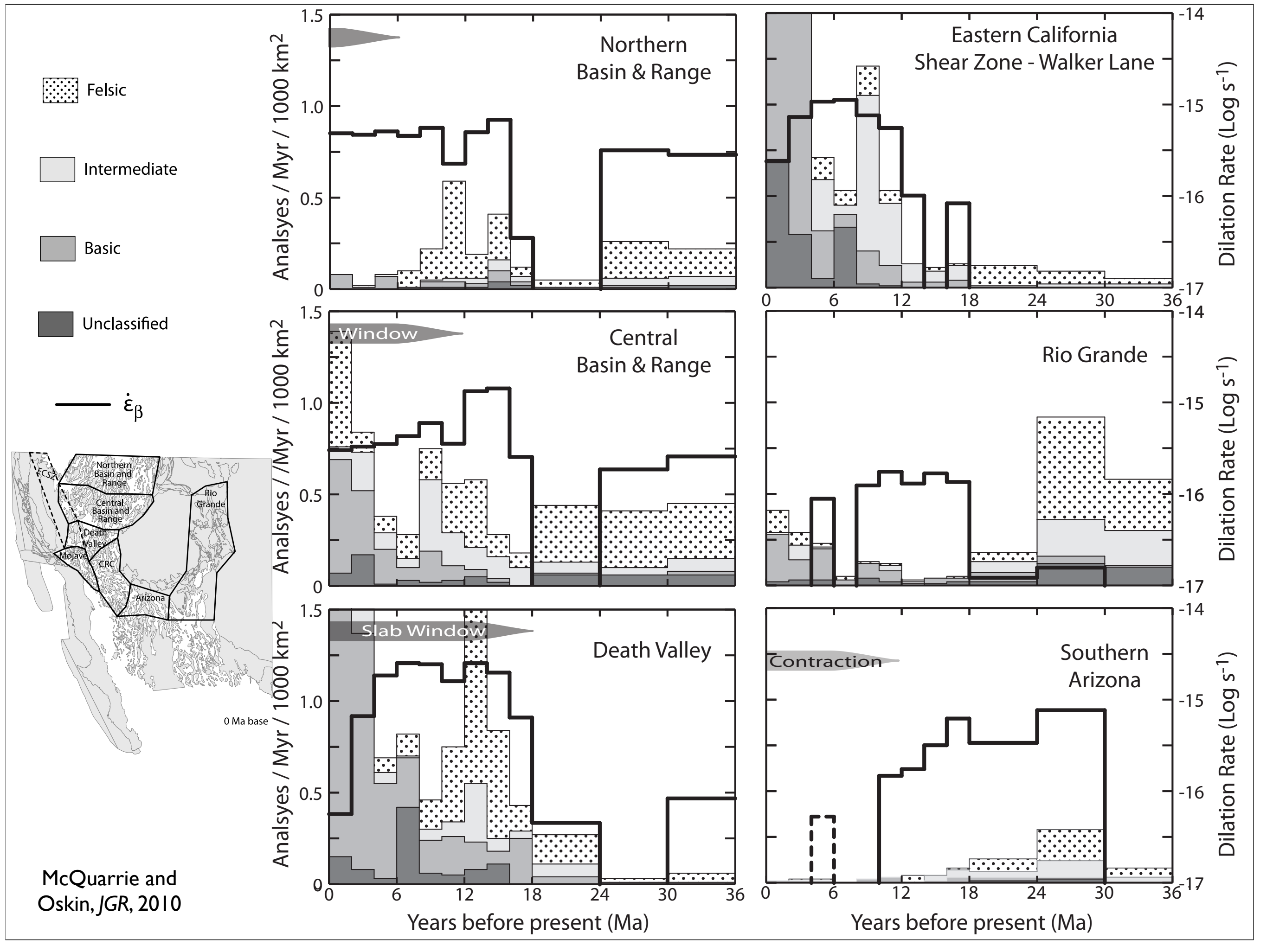

Recall these are not volumes….

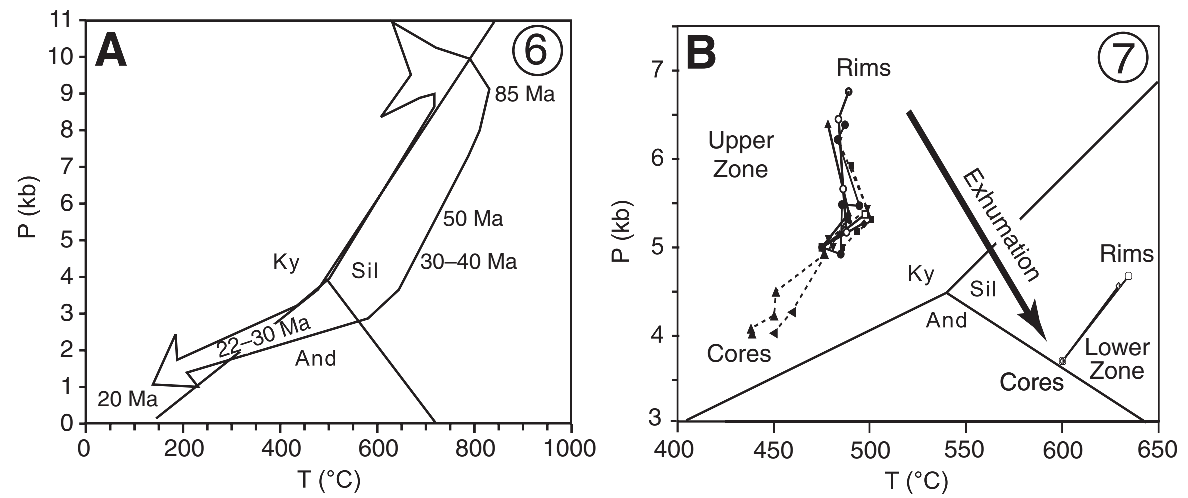

Figure 4. P-T paths from Great Basin core complexes. (A) P-T-t path envelope determined from an array of individual P-T determinations from metabasite and metapelite of the East Humboldt Range, from McGrew et al. (2000). Interpreted decompression is corroborated by decompressional metamorphic reaction textures. (B) P-T paths from schist of Stevens Spring from the northern Grouse Creek Mountains, northwestern Utah (location R, Fig. 1). Paths from Hoisch et al. (2002) are shown as solid lines, and paths from Harris et al. (2007) are shown as dashed lines. Samples came from two zones within the schist of Stevens Spring, upper and lower, as shown, corresponding to different garnet growth reactions. Al_2SiO_5 polymorphic transformations are shown in solid lines (Pattison, 1992); Ky—kyanite; Sil—sillimanite; And—andalusite. Paths were determined from simulations of garnet growth zoning, using the Gibbs method on the basis of Duhem's theorem (e.g., Spear et al., 1991). Numbers in the upper right corners of both panels refer to location numbers shown in Figure 1.

WELLS & HOISCH, GSA BULL 2008

Reminder of some of the later stage exhumation of rocks—these are found in ranges termed core complexes

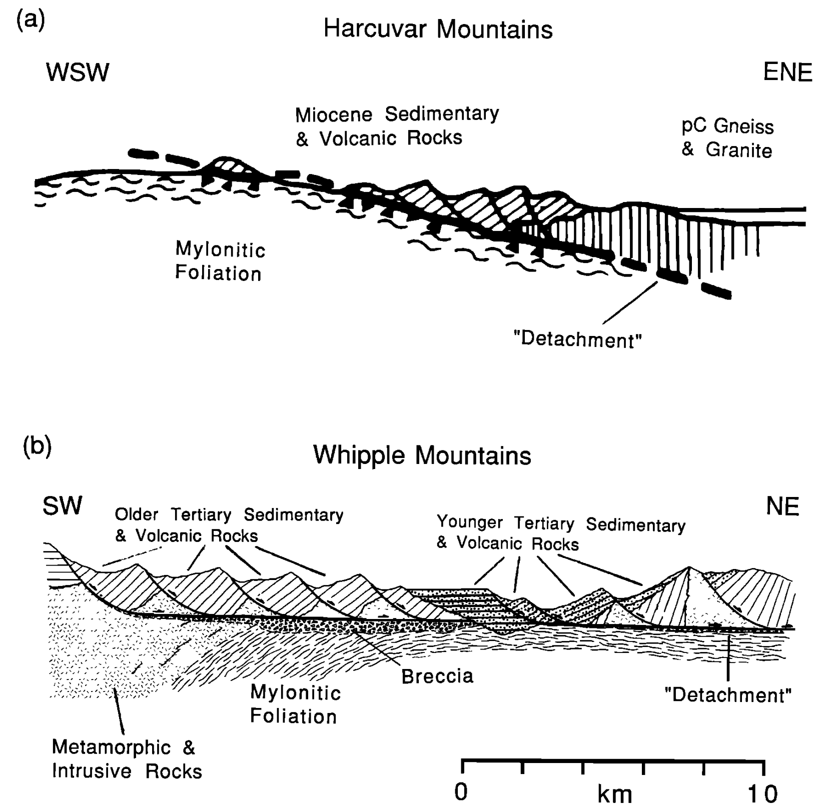

Fig. 1. Interpretative cross sections of two metamorphic core complexes showing features common to many core complexes: (a) the Harcuvar Mountains in Arizona [after Rehrig and Reynolds, 1980] and (b) the Whipple Mountains in California with inferred doming removed [after Davis, 1980].

Buck, Tectonics, 1988

Generic core complex

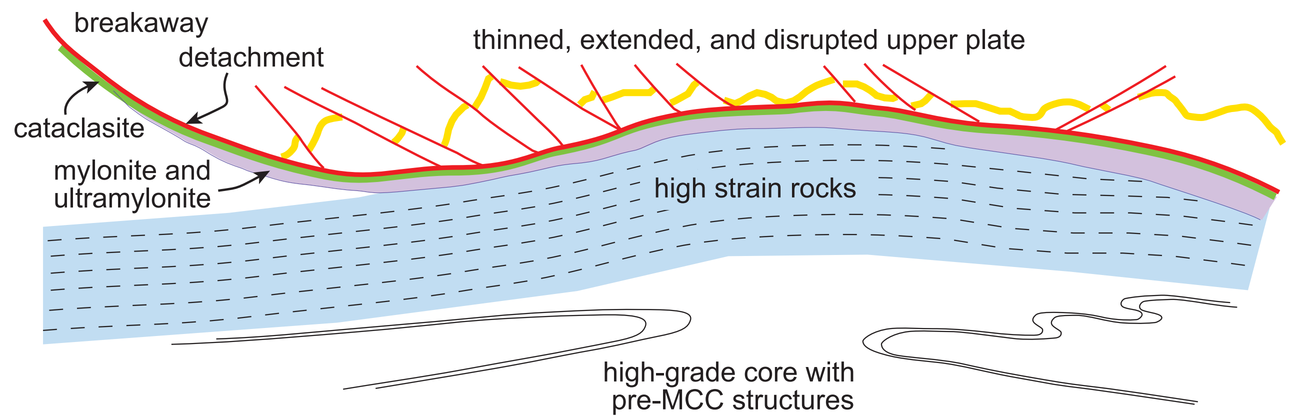

Platt, *J. Geol. Soc.*, 2015

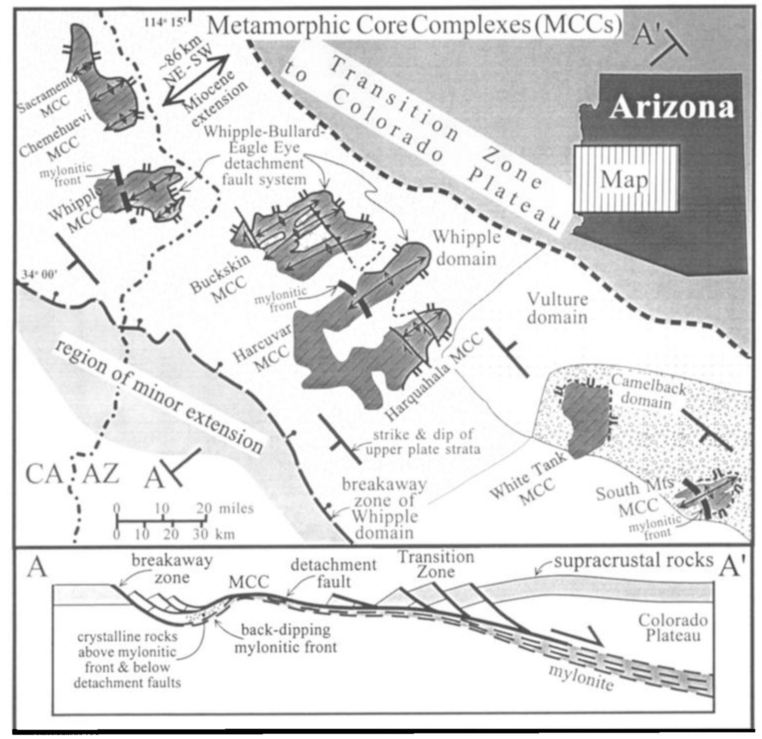

Figure 1. Location map, generalized geologic map and cross section (A - A') of metamorphic core complexes (MCCs) of west central Arizona and southeastern California [after *Reynolds et al*., 1988]. The Harquahala, Harcuvar, Buckskin, Whipple, Chemehuevi, Sacramento, White Tank, and South Mountains MCCs represent antiformal arches of mylonitized footwall rocks. Normal-slip, low-angle (dip of 10° - 25°) detachment faults separate MCC footwall rocks from tilted, hanging wall strata. The Camelback, Vulture, and Whipple domains represent areas of similar regional dip of hanging wall strata [*Reynolds et a*l., 1988]. MCC footwalls and titled hanging wall strata form a zone of large-magnitude Miocene extension separating regions that experienced little Miocene extension. These little extended regions include the "Transition Zone to the Colorado Plateau" and the "region of only minor extension" southwest of the Whipple domain breakaway zone.

Livaccari and Geissman, Tectonics, 2001

These structures also vary in map view, making doubly-plunging antiforms. Look at one of these (Buckskin) in more detail

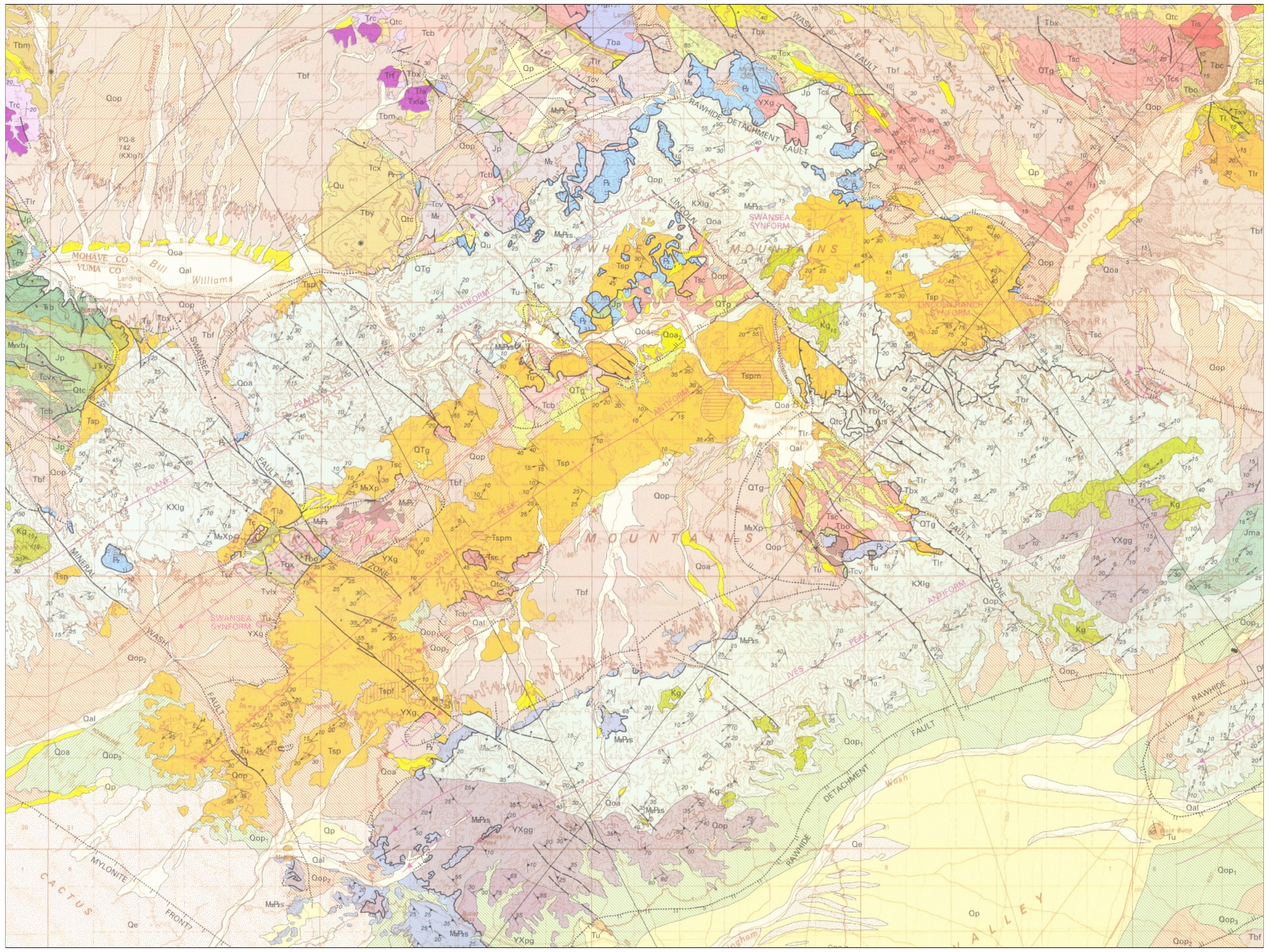

Blue in upper right upper plate. Orange is lower plate T pluton, purple at bottom lower plate pC.

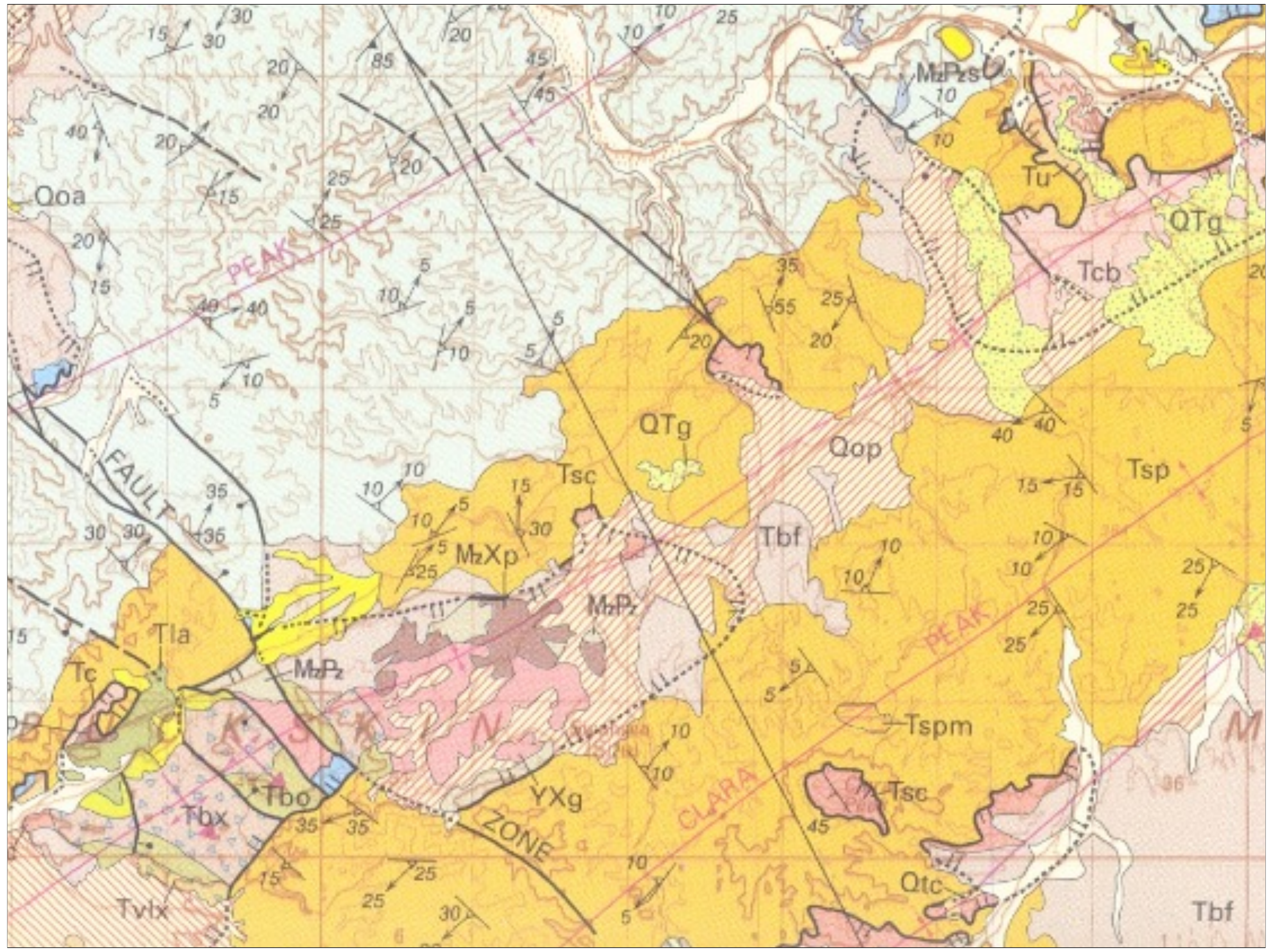

Qoa
PEAK
FAULT
ZONE
CLARA
PEAK
QTg
Tsc
M2Xp
M2P2
Qop
Tbf
Tsp
Tu
QTg
Tcb
M2P2s
Tla
Tc
Tbx
Tbo
YXg
Tspm
Tsc
Qtc
Tbf
Tvlx

Rawhide Mtns from Swansea site

Red vs green, Buckskin CC

Looking into the fault

Mylonite, Buckskin Mtns

Catalina Mtns, So. AZ

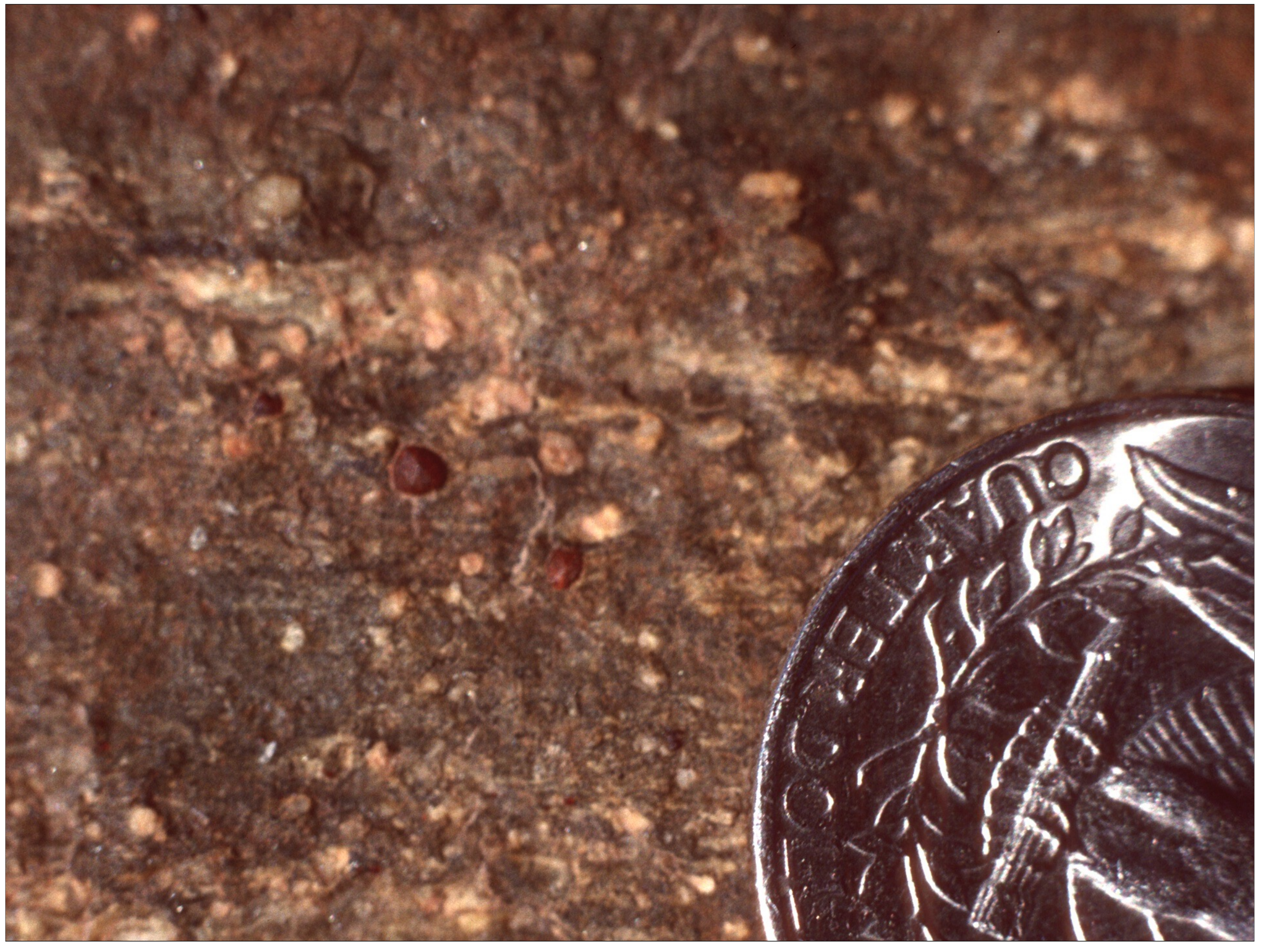

Cataclasite?

Ultramylonite, Catalina core complex (Rincon Mtns)

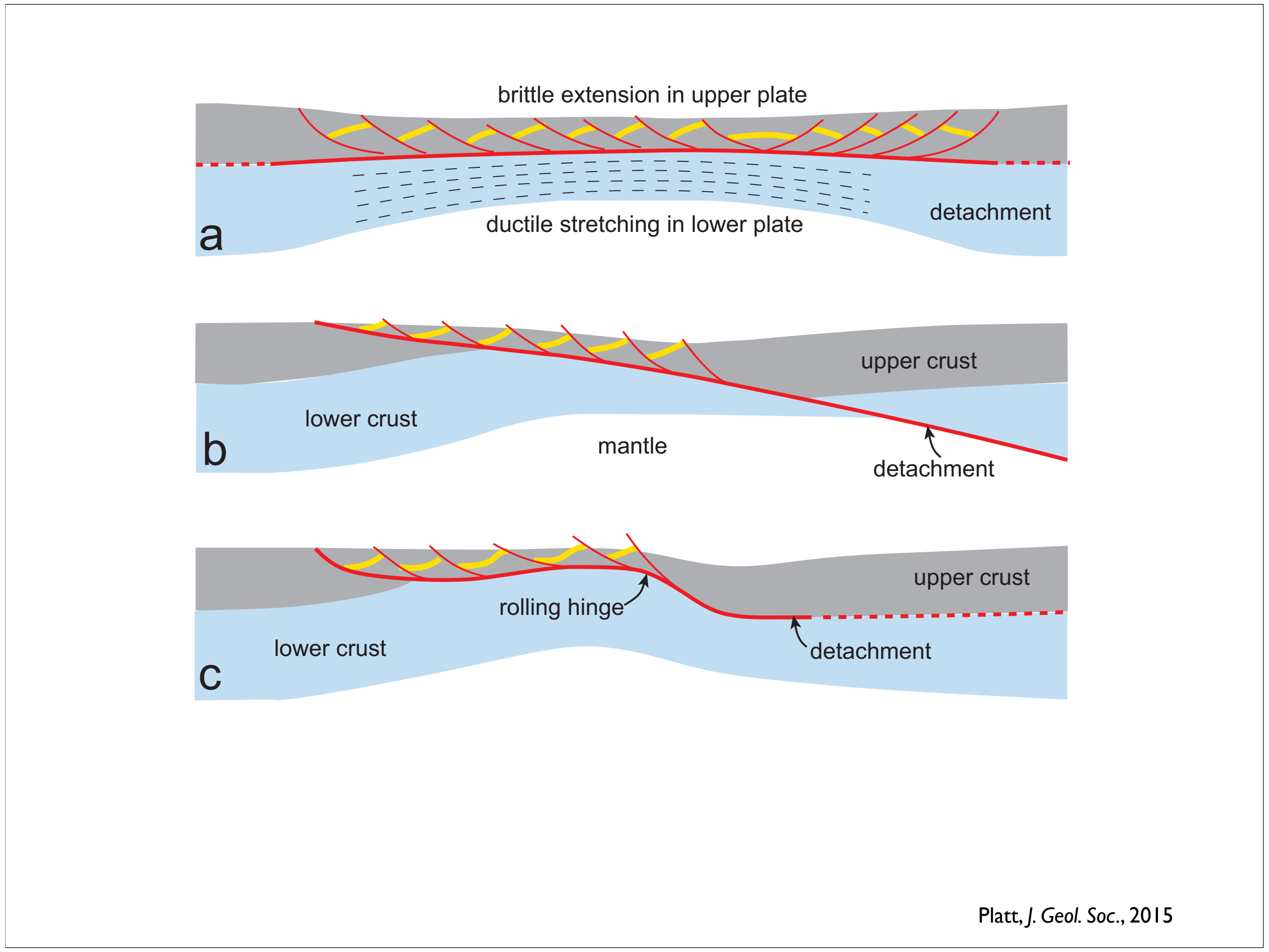

So how are these things created? Simple cartoons of some ideas. Look at what the observations were that led to these.

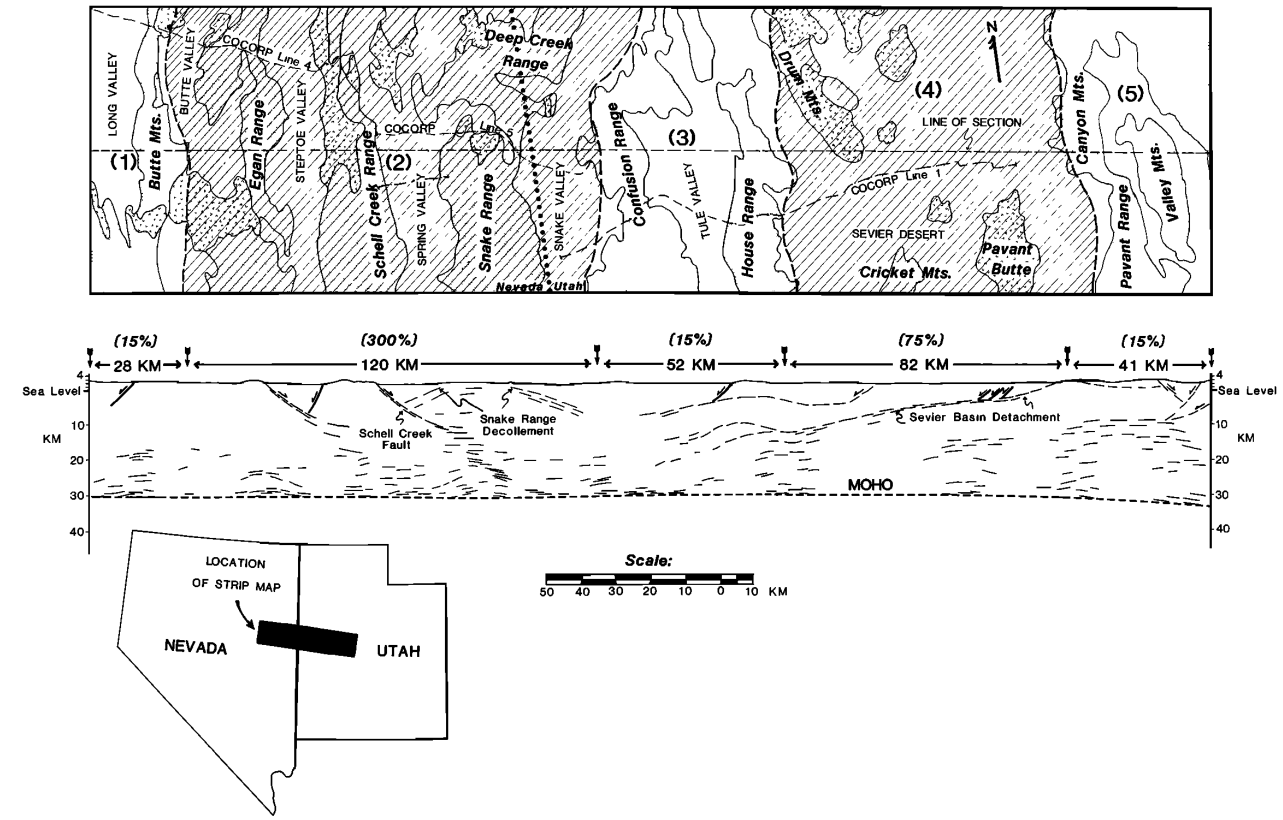

Fig. 1. Geologic strip map and generalized crustal cross section across the eastern Great Basin. Geologic map modified from Stewart and Carlson [1978] and Hintze [1980] Stippled areas represent Precambrian to Mesozoic carbonate and clastic rocks, and v represent Tertiary and Quaternary volcanic rocks. Numbered areas correspond to domain discussed in text, with the more highly extended domains highlighted with slanted lines. Subsurface information shown on the cross section is drawn largely from the seism reflection profiles described by Allmendinger et al. [1983], Hauser et al. [1984], Gans et al. [1985], McCarthy [1986], and Klemperer et al. [1986]. Depth to the reflection M was calculated assuming an average crustal velocity of 6.5 km/s.

Gans, Tectonics, 1987

First up, recognition of very variable amounts of extension but flat Moho.

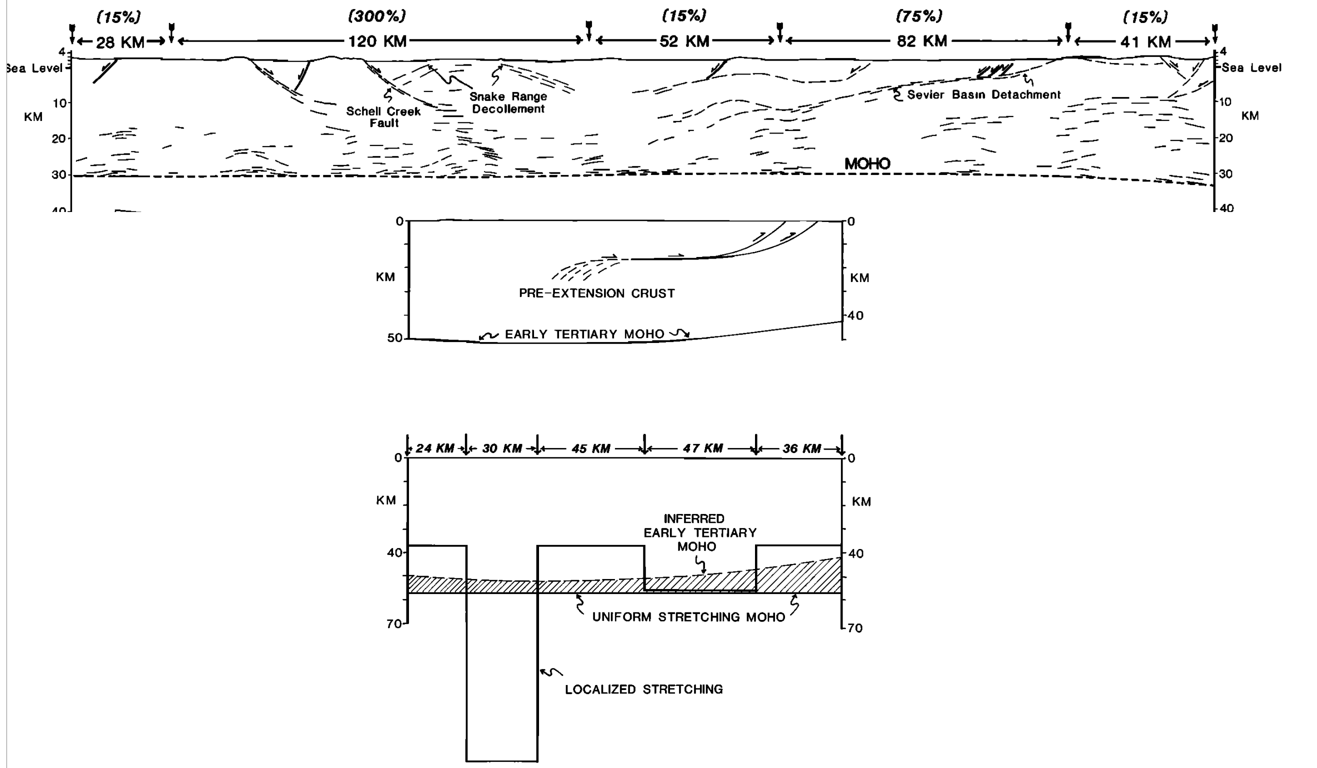

Fig. 2. (A) The inferred crustal thickness profile of the eastern Great Basin prior to the onset of extensional tectonism, as deduced from regional geological considerations and a comparison with the Canadian Cordillera. Note that the E-W dimension corresponds to the width of the transect discussed in the text after the effects of Cenozoic extension are removed. (B) The predicted preextensional Moho of the eastern Great Basin calculated using two different models for crustal stretching, neither of which incorporates additions of new material to the crust. The Localized Stretching Moho assumes pure shear of the crustal column beneath each domain by an amount equivalent to the percent extension measured at the surface. The Uniform Stretching Moho assumes pure shear of the eastern Great Basin by the average amount of extension measured across the entire transect. The hatchured area represents the amount of new material that is inferred to have been added to the crust during Tertiary stretching. See text for discussion.

Gans, *Tectonics*, 1987

You push things back assuming vertically uniform deformation and you get craziness. [Note that broader section near here by

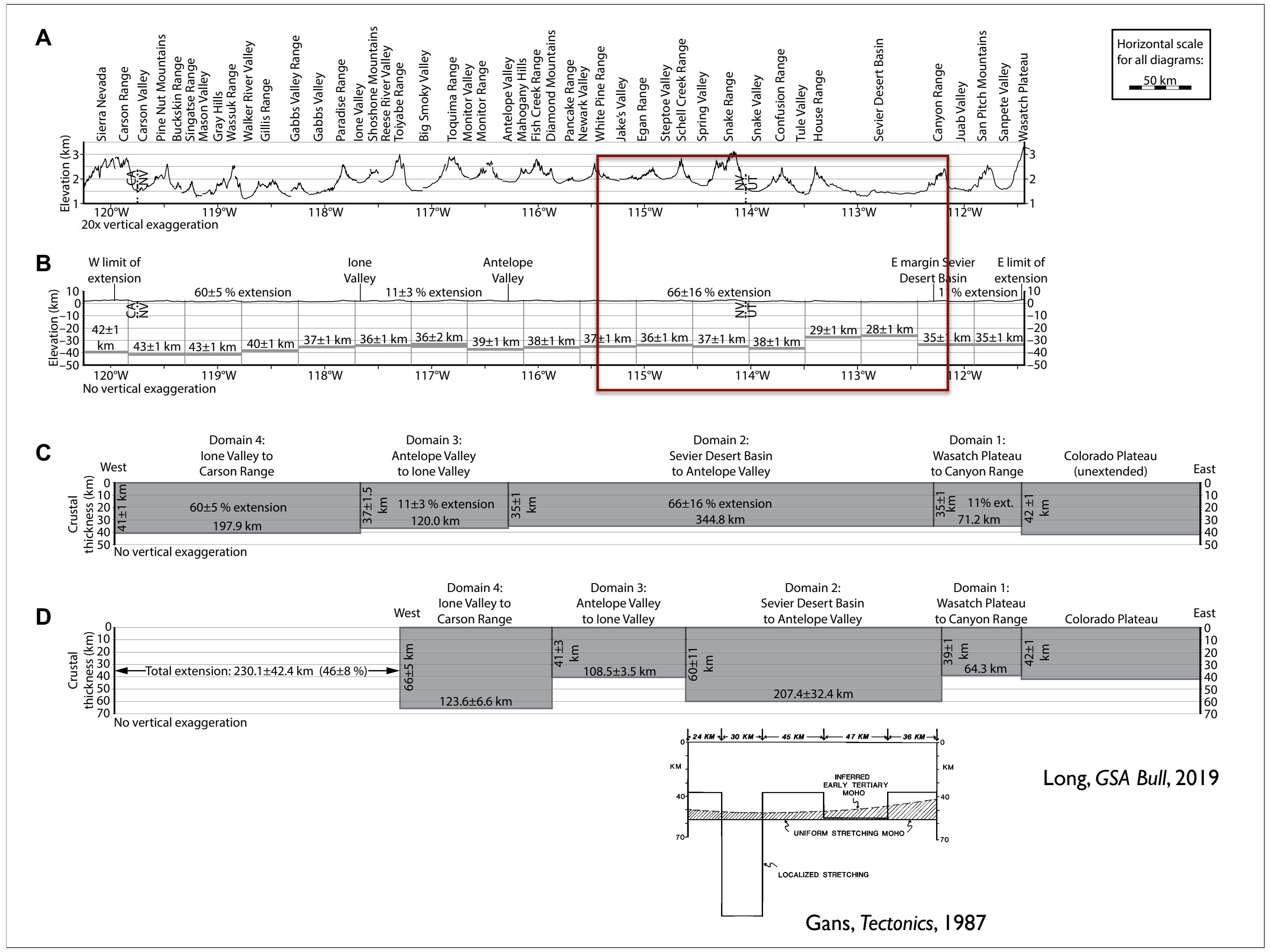

Somewhat similarly if you step back to a larger scale and allow averaging over larger areas, still get some peculiar variations.

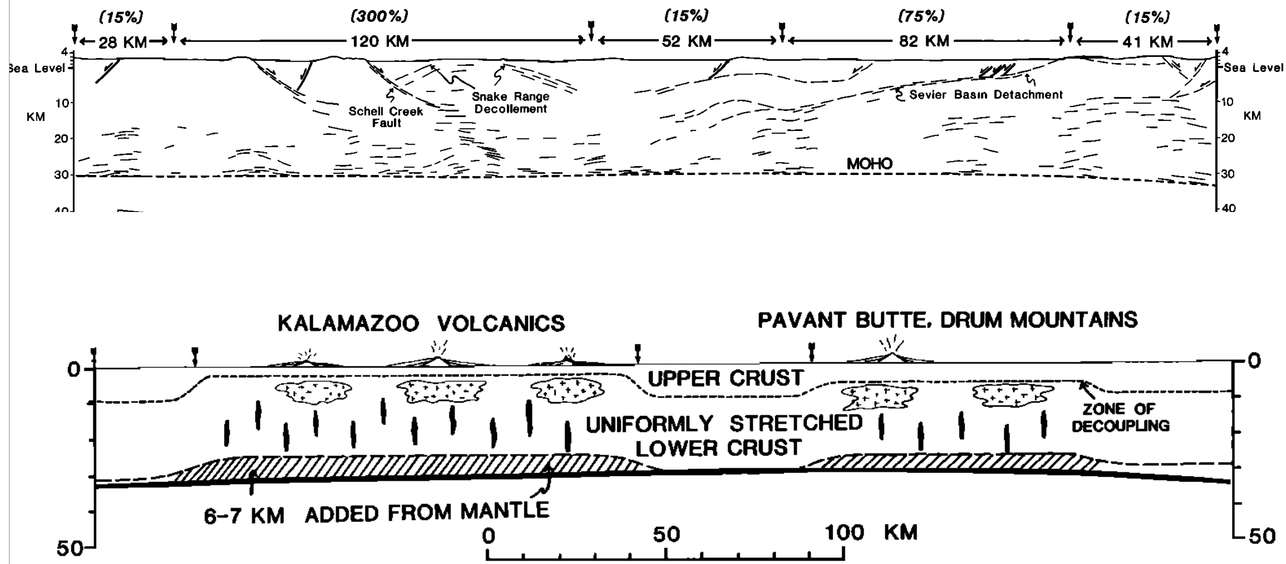

Fig. 3. A highly generalized present-day cross section of the eastern Great Basin that illustrates the two-layer, open-system model for crustal stretching. See text for discussion.

Gans, Tectonics, 1987

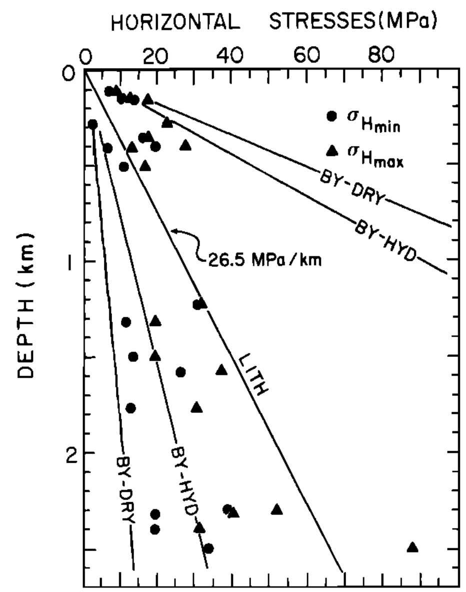

Fig. 1. Total horizontal stresses measured in southern Africa [*McGarr and Gay,* 1978]. The vertical total stress gradient (26.5 MPa/km) is shown along with Byerlee's law (BY) for hydrostatic pore pressure (HYD) and zero pore pressure (DRY).

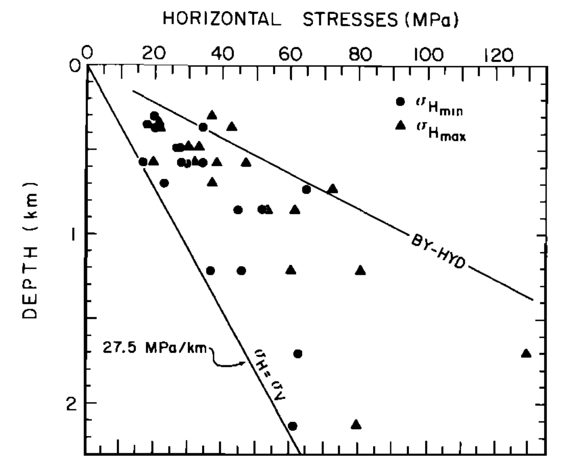

Fig. 3. Total horizontal stresses measured in Canada [*McGarr and Gay,* 1978]. Symbols as in Figure 1.

Brace & Kohlstedt,, JGR, 1980

$$\dot{\epsilon} = 7 \times 10^4 (\sigma_1 - \sigma_3)^3 \exp\left(\frac{-0.52 \text{ MJ/mol}}{RT}\right) \qquad \sigma_1 - \sigma_3 < 200 \text{ MPa}$$

$$\dot{\epsilon} = 5.7 \times 10^{11} \exp\left[\frac{-0.54 \text{ MJ/mol}}{RT}\left(1 - \frac{\sigma_1 - \sigma_3}{8500}\right)^2\right] \qquad \sigma_1 - \sigma_3 > 200 \text{ MPa} \tag{4}$$

where $\dot{\epsilon}$ is in s^{-1} and $\sigma_1 - \sigma_3$ is in megapascals. The plastic deformation behavior of quartz appears to depend markedly on OH^- content. We consider here experimental results on dry samples which should provide an upper limit to the strength of quartzite. Recent experiments of *Christie et al.* [1979] on dry quartzite at 800° and 900°C combined with the data of *Heard and Carter* [1968] yield the flow law

$$\dot{\epsilon} = 5 \times 10^6 (\sigma_1 - \sigma_3)^3 \exp\left(\frac{-0.19 \text{ MJ/mol}}{RT}\right) \qquad \sigma_1 - \sigma_3 < 1000 \text{ MPa} \tag{5}$$

where $\dot{\epsilon}$ is in s^{-1} and $\sigma_1 - \sigma_3$ is in megapascals.

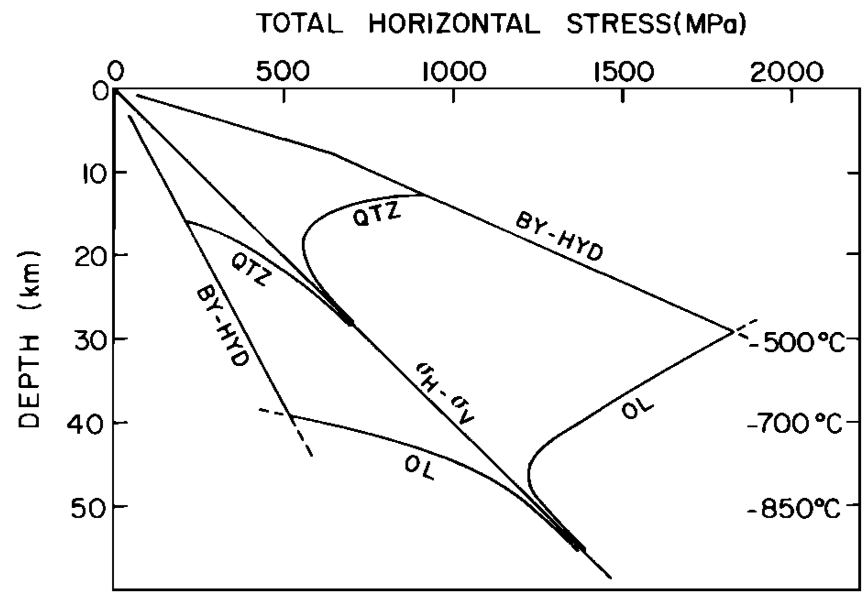

Fig. 4. Limiting values of total horizontal stress as a function of depth, based on Byerlee's law with hydrostatic pore pressure (BY-HYD) and the quartz (QTZ) and olivine (OL) flow laws adjusted to a strain rate of 10^{-15} s^{-1}. The temperature profile $T(°K) = 350 + 15z(km)$.

Brace & Kohlstedt,, JGR, 1980

$$\dot{\epsilon} = 7 \times 10^4 (\sigma_1 - \sigma_3)^3 \exp\left(\frac{-0.52 \text{ MJ/mol}}{RT}\right)$$

$$\sigma_1 - \sigma_3 < 200 \text{ MPa}$$

$$\dot{\epsilon} = 5.7 \times 10^{11} \exp\left[\frac{-0.54 \text{ MJ/mol}}{RT}\left(1 - \frac{\sigma_1 - \sigma_3}{8500}\right)^2\right] \tag{4}$$

$$\sigma_1 - \sigma_3 > 200 \text{ MPa}$$

where $\dot{\epsilon}$ is in s^{-1} and $\sigma_1 - \sigma_3$ is in megapascals. The plastic deformation behavior of quartz appears to depend markedly on OH^- content. We consider here experimental results on dry samples which should provide an upper limit to the strength of quartzite. Recent experiments of *Christie et al.* [1979] on dry quartzite at 800° and 900°C combined with the data of *Heard and Carter* [1968] yield the flow law

$$\dot{\epsilon} = 5 \times 10^6 (\sigma_1 - \sigma_3)^3 \exp\left(\frac{-0.19 \text{ MJ/mol}}{RT}\right) \tag{5}$$

$$\sigma_1 - \sigma_3 < 1000 \text{ MPa}$$

where $\dot{\epsilon}$ is in s^{-1} and $\sigma_1 - \sigma_3$ is in megapascals.

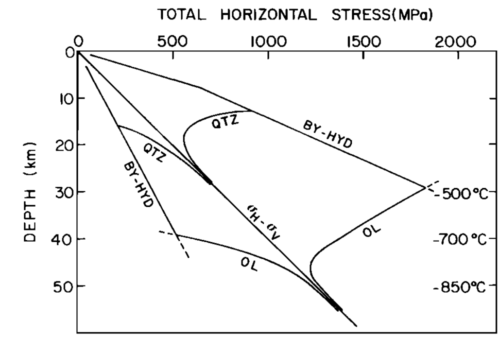

Fig. 4. Limiting values of total horizontal stress as a function of depth, based on Byerlee's law with hydrostatic pore pressure (BY-HYD) and the quartz (QTZ) and olivine (OL) flow laws adjusted to a strain rate of 10^{-15} s^{-1}. The temperature profile $T(°K) = 350 + 15z$(km).

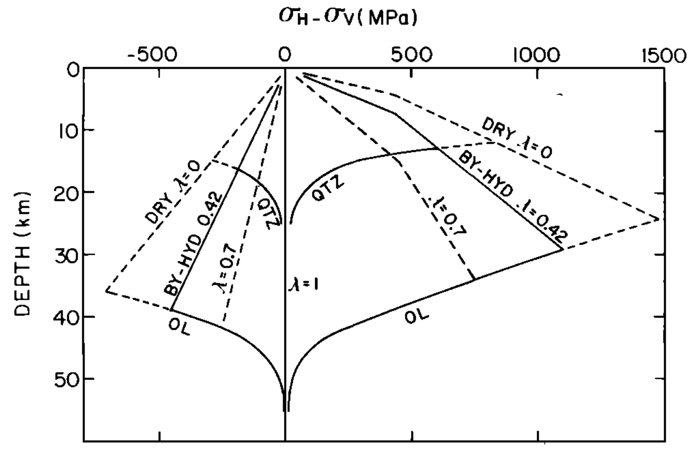

Brace & Kohlstedt,, JGR, 1980

Fig. 5. Difference between maximum or minimum horizontal stress and the vertical stress as a function of depth. Values of λ give pore pressure level. See also Figure 4.

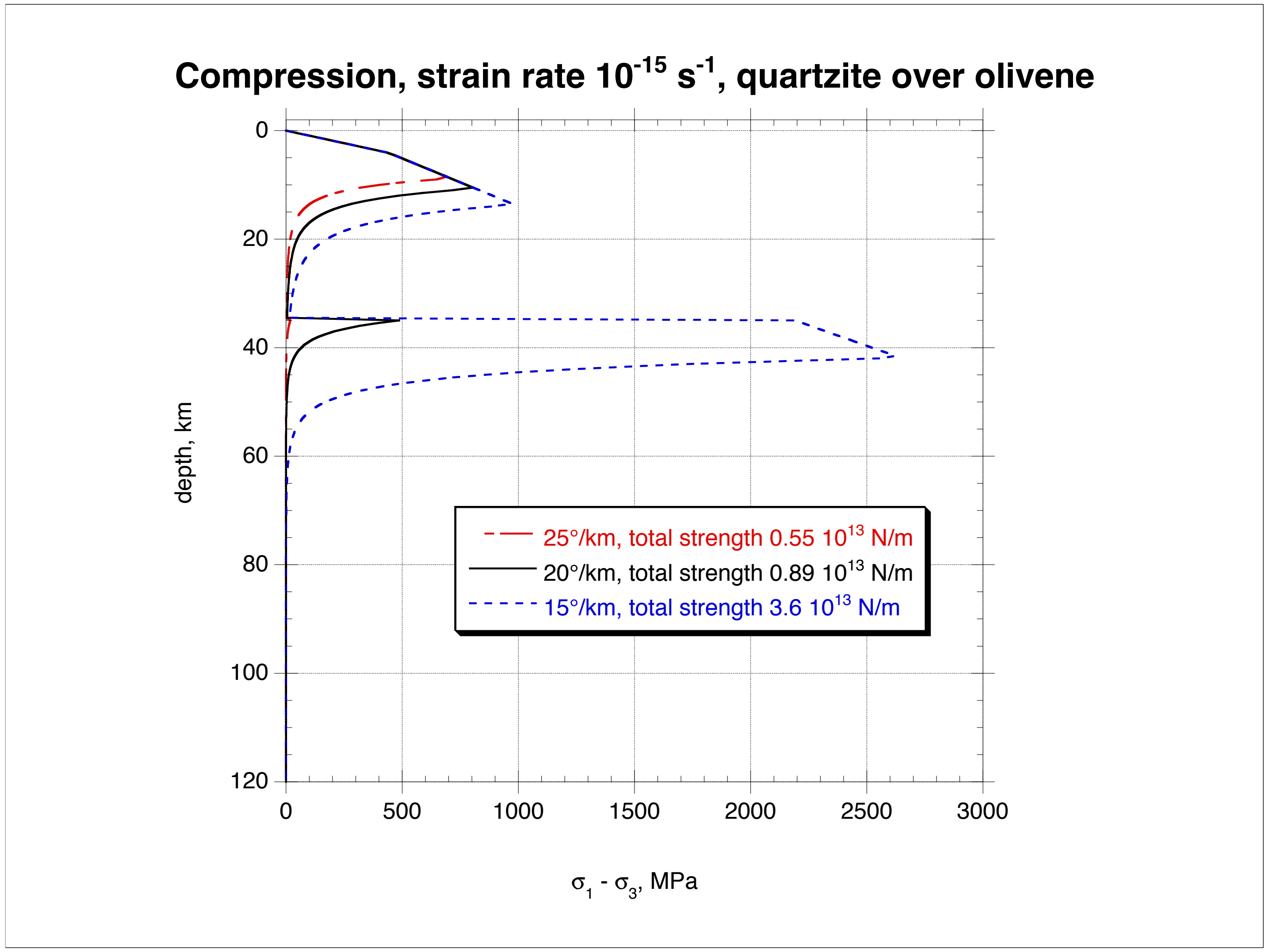
Compression, strain rate 10^{-15} s^{-1}, quartzite over olivene
depth, km
0
20
40
60
80
100
120
0
500
1000
1500
2000
2500
3000
$\sigma_1 - \sigma_3$, MPa
25°/km, total strength 0.55 10^{13} N/m
20°/km, total strength 0.89 10^{13} N/m
15°/km, total strength 3.6 10^{13} N/m

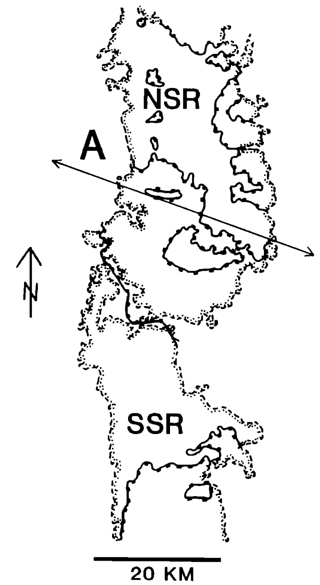

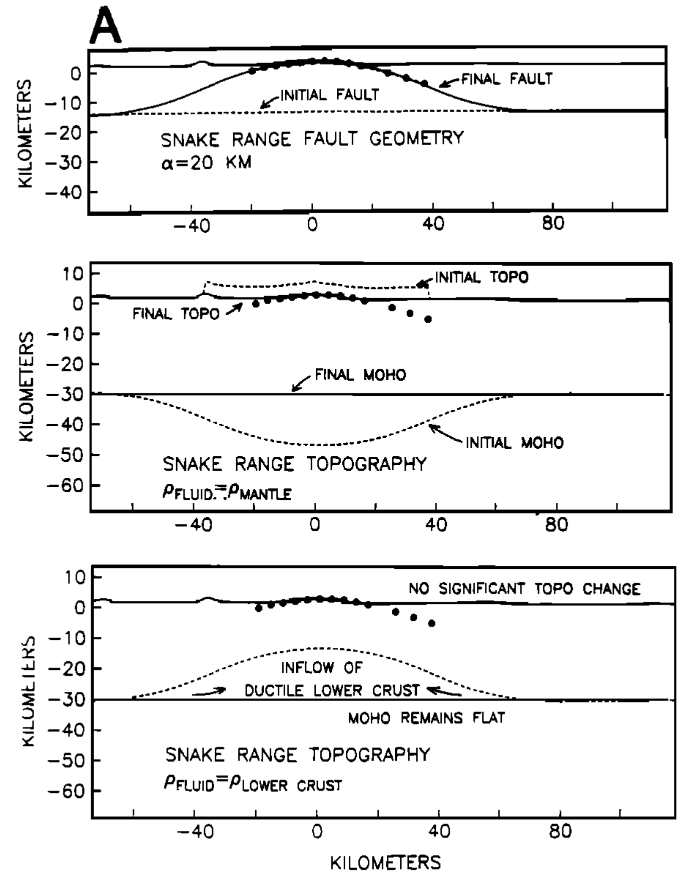

Fig. 3. Pre- and post-extensional fault geometry and topography for the Snake Range and Whipple Mountain detachment faults assuming that the fault was initially flat at a depth of 14 km (Figures 3a and 3c) or had an initial depth of 14 km at x=0 and dipped 20° E between the surface and 30 km depth (Figures 3b and 3d). Observed fault geometries (dots) and observed topography (solid lines) are shown in each panel (locations in Figure 2). Top panels in each Figure 3a-3d show the assumed initial (dashed line) and computed final (solid line) fault geometries.

Block and Royden, Tectonics, 1990

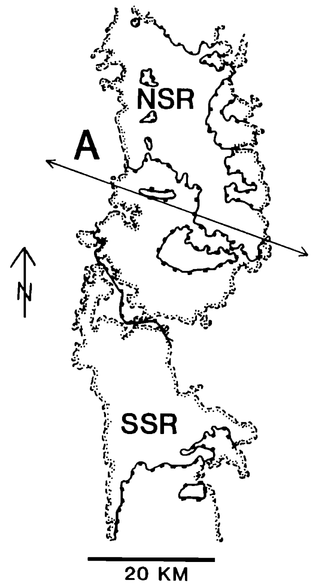

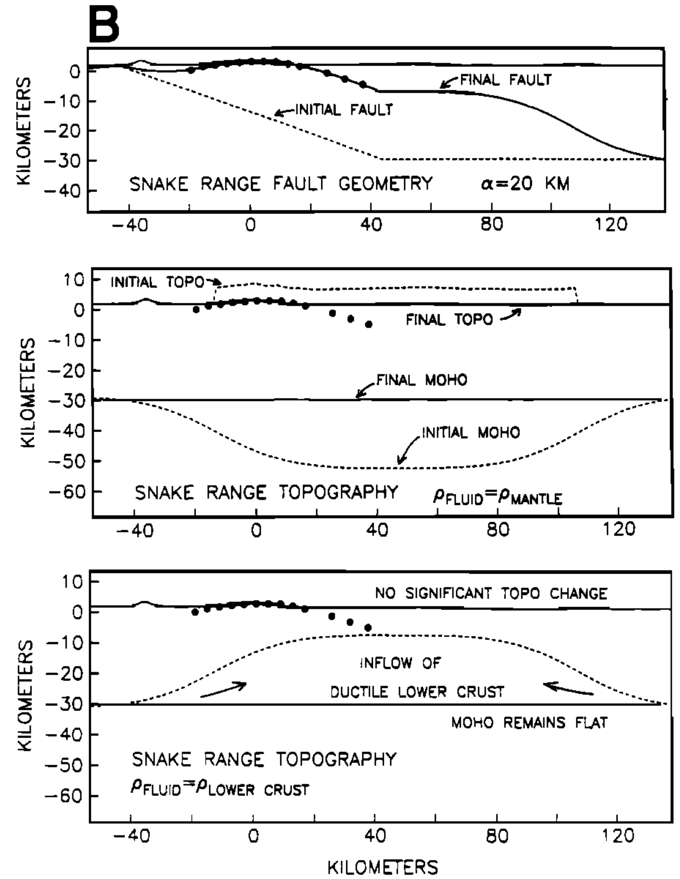

Fig. 3. Pre- and post-extensional fault geometry and topography for the Snake Range and Whipple Mountain detachment faults assuming that the fault was initially flat at a depth of 14 km (Figures 3a and 3c) or had an initial depth of 14 km at x=0 and dipped 20° E between the surface and 30 km depth (Figures 3b and 3d). Observed fault geometries (dots) and observed topography (solid lines) are shown in each panel (locations in Figure 2). Top panels in each Figure 3a-3d show the assumed initial (dashed line) and computed final (solid line) fault geometries.

Block and Royden, Tectonics, 1990

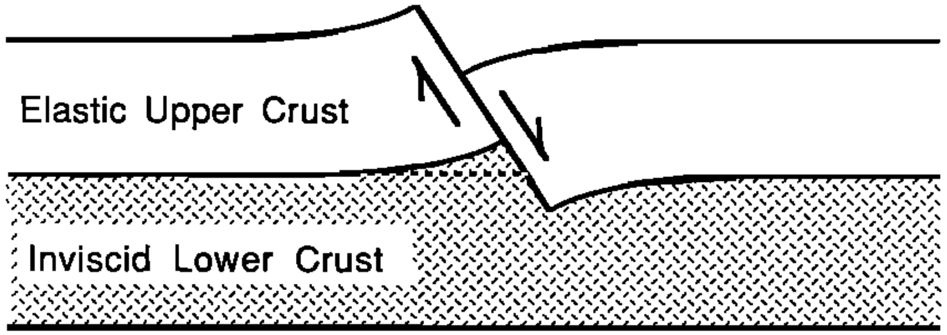

Fig. 4. Schematic of a normal fault cutting the entire upper crust. The base of the upper crust is always at a fixed depth, as shown by the dashed line.

Buck, Tectonics, 1988

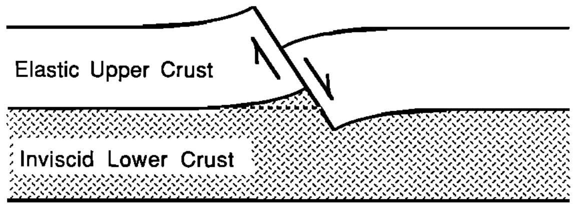

Fig. 4. Schematic of a normal fault cutting the entire upper crust. The base of the upper crust is always at a fixed depth, as shown by the dashed line.

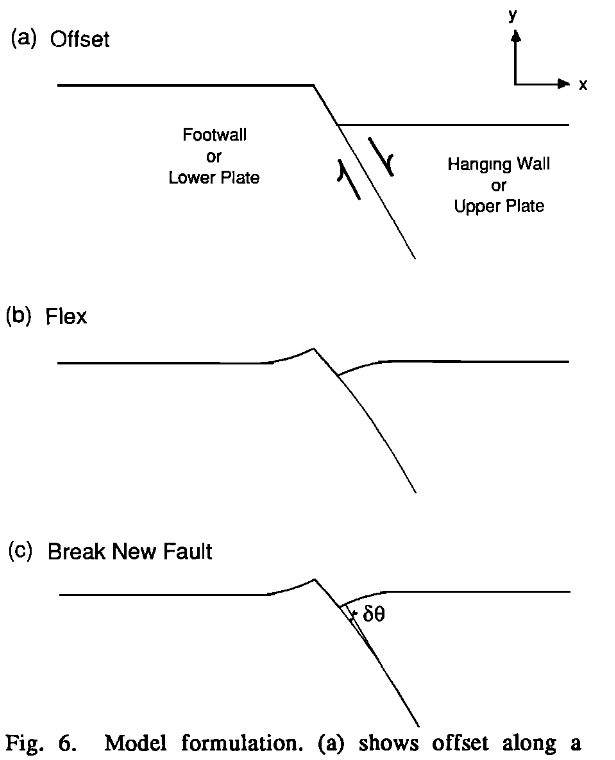

Fig. 6. Model formulation. (a) shows offset along a high-angle normal fault; (b) shows flexural response to the topographic load caused by the offset. The flexure causes rotation of the high angle normal fault over a flexural wavelength. In (c) the rotated fault is abandoned and a new extension of the fault, which is rooted in the lower crust, is cut through the top of the upper crust.

Buck, Tectonics, 1988

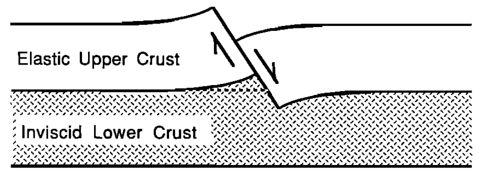

Fig. 4. Schematic of a normal fault cutting the entire upper crust. The base of the upper crust is always at a fixed depth, as shown by the dashed line.

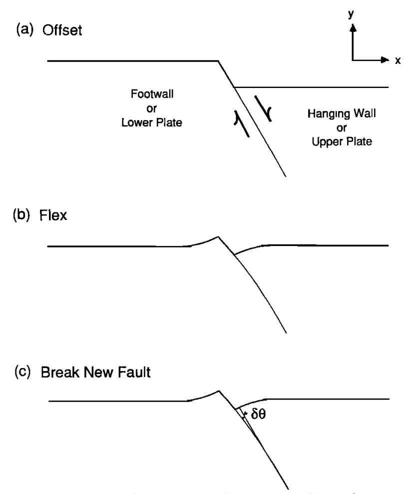

Fig. 6. Model formulation. (a) shows offset along a high-angle normal fault; (b) shows flexural response to the topographic load caused by the offset. The flexure causes rotation of the high angle normal fault over a flexural wavelength. In (c) the rotated fault is abandoned and a new extension of the fault, which is rooted in the lower crust, is cut through the top of the upper crust.

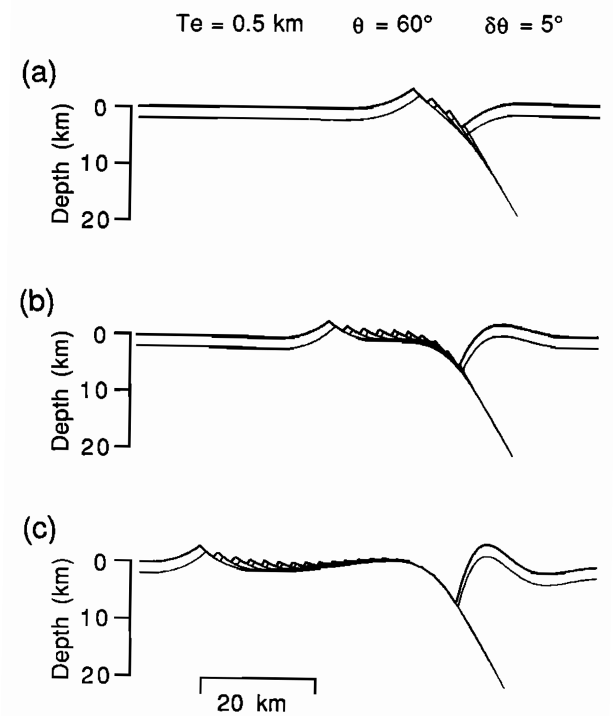

Fig. 7. Topography and positions of active and abandoned faults resulting from a calculation with a fault angle θ of 60°, an effective flexural rigidity of 0.5 km, and a rotation angle δθ of 5°. A line at 2 km depth is also plotted. Horizontal offsets of approximately (a) 15 km, (b) 30 km, and (c) 60 km are shown. There is no vertical exaggeration.

Buck, Tectonics, 1988

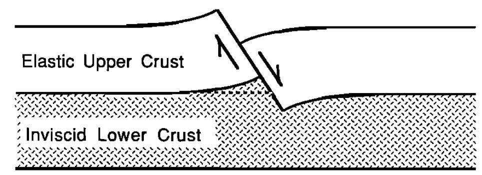

Fig. 4. Schematic of a normal fault cutting the entire upper crust. The base of the upper crust is always at a fixed depth, as shown by the dashed line.

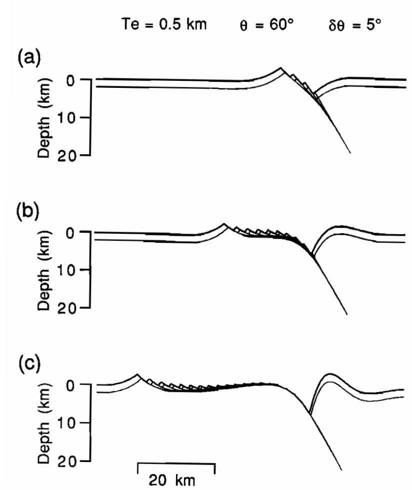

Fig. 7. Topography and positions of active and abandoned faults resulting from a calculation with a fault angle θ of 60°, an effective flexural rigidity of 0.5 km, and a rotation angle δθ of 5°. A line at 2 km depth is also plotted. Horizontal offsets of approximately (a) 15 km, (b) 30 km, and (c) 60 km are shown. There is no vertical exaggeration.

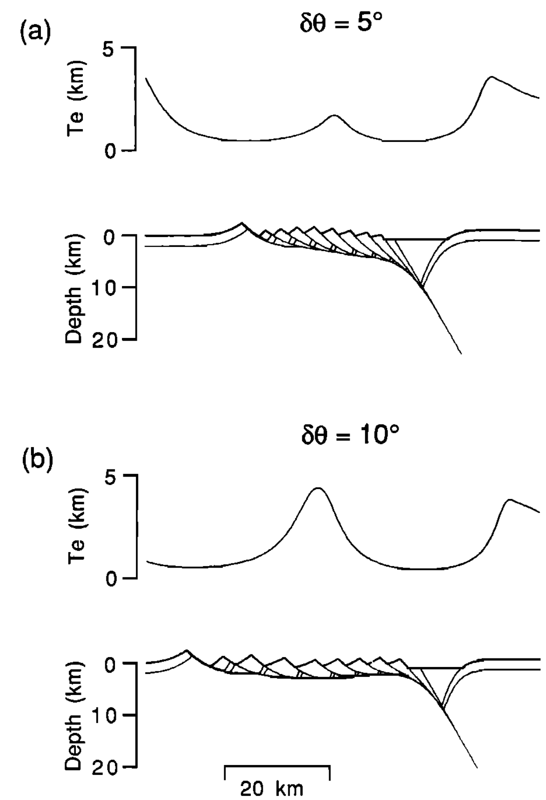

Fig. 12. Results of variable rigidity calculations in which sediment has been added to fill in all levels below 1000 m depth. Two cases of assumed angle of fault rotation before fault abandonment are shown: δθ = 5° and δθ = 10°.

Buck, Tectonics, 1988

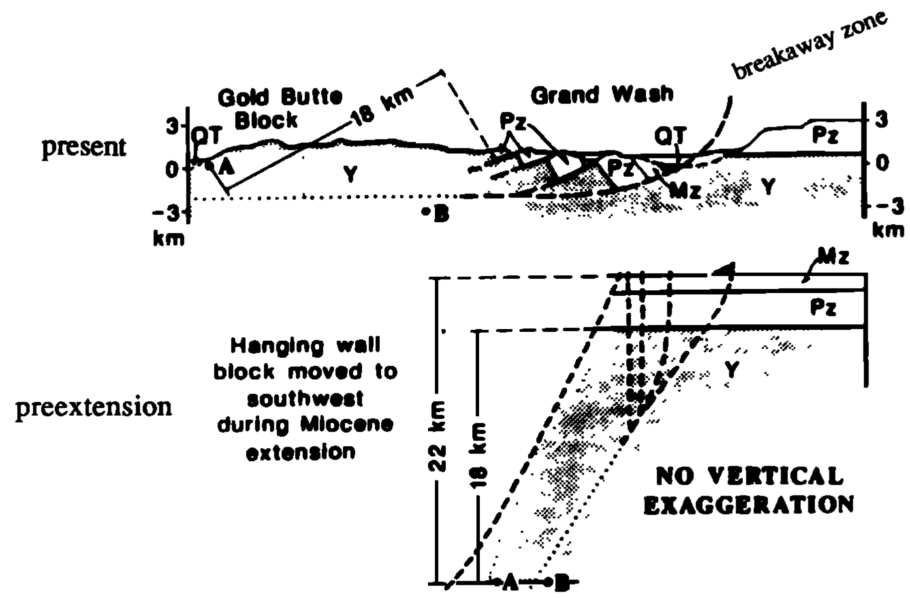

Fig. 2. Schematic cross section perpendicular to strike of transition zone at the latitude of Lake Mead showing inferred uplift of Gold Butte block. Location of profile shown in Figure 1. Modified from *Wernicke and Axen* [1988].

Kruse et al., JGR, 1991

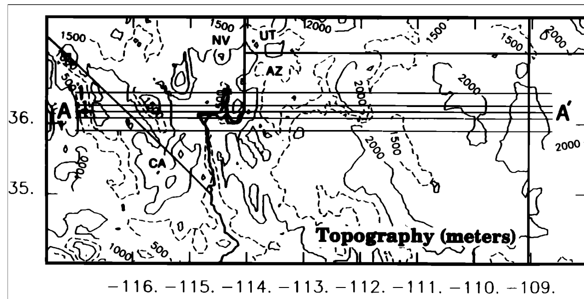

Fig. 3a. Topographic map of Lake Mead area and western Colorado Plateau. Thick lines mark state boundaries and the shore of Lake Mead. Thin straight lines show the location of topography profiles in Figure 4. Data taken from the NOAA TGP–0030 30' topography data set.

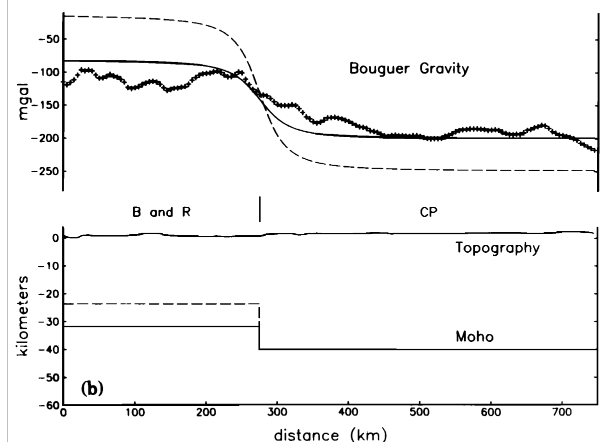

Fig. 5. (continued)

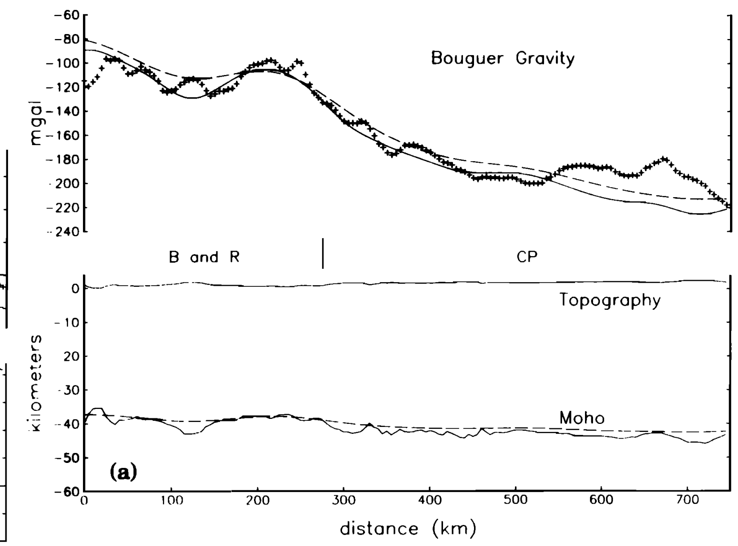

Fig. 5. Bouguer gravity anomalies predicted by simple compensation models. Topography data used in modeling are averaged from the five profiles of Figure 4. Crosses mark observed Bouguer gravity anomalies similarly averaged from the profiles of Figure 4. Short vertical line between upper and lower plots marks location of transition zone. *(a)* Solid curve shows local (Airy) compensation of topography by deflections of the Moho. Dashed curve shows compensation at Moho assuming a flexural rigidity of 10^{22} N m. *(b)* Bouguer gravity anomalies and Moho depths corresponding to uniform stretching of the lithosphere west of the transition zone according to the model of *McKenzie* [1978]. Solid curves indicate values associated with extension by a factor $\beta = 1.33$, resulting in 10 km of crustal thinning of crust initially 40 km thick. Dashed curves show values predicted from extension by a factor of 2 with 20 km of crustal thinning. Bouguer gravity anomalies are calculated assuming that the lithosphere in the extended region has thinned uniformly, maintaining a linear temperature gradient between the surface and a temperature of 1350°C at the base of the lithospheric plate. The unextended thickness of the lithospheric plate is set to 125 km. Deflections of the Moho maintain local (Airy) isostasy. To best fit the observed gravity data –200 mGal were added to the gravity predicted by the model for $\beta = 1.33$ (solid curves) and 250 mGal were added to the gravity predicted by the $\beta = 2$ (dashed curves) model.

Kruse et al., JGR, 1991

I think they assumed a Moho contrast of 600 kg m^{-3}

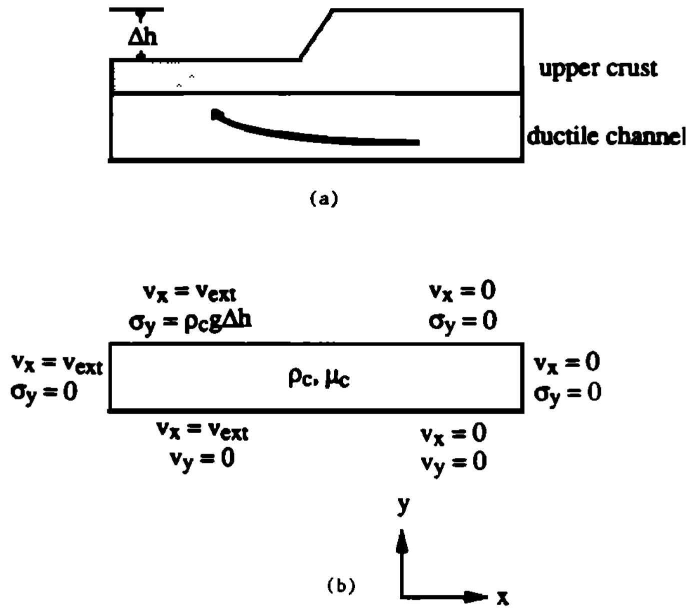

Fig. 7. *(a)* Schematic representation of ductile flow in response to uppe crustal thinning. *(b)* Boundary conditions on finite element models for ductile channel with a fixed lower boundary.

Kruse et al., JGR, 1991

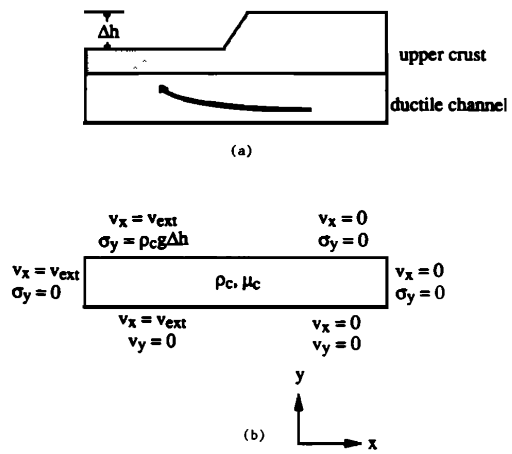

Fig. 7. (*a*) Schematic representation of ductile flow in response to uppe crustal thinning. (*b*) Boundary conditions on finite element models for ductile channel with a fixed lower boundary.

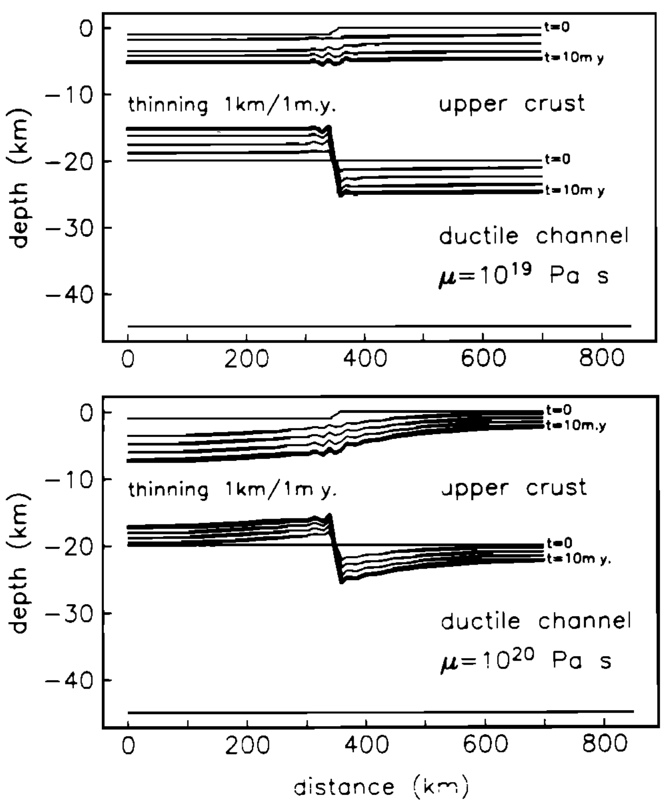

Fig. 10. Variations in total crustal thickness and ductile channel thickness for flow in a channel initially 25 km thick with a fixed lower boundary. The upper crust has zero flexural rigidity and thins over the left side of the mesh at a rate of 1 km/m.y.

Kruse et al., JGR, 1991

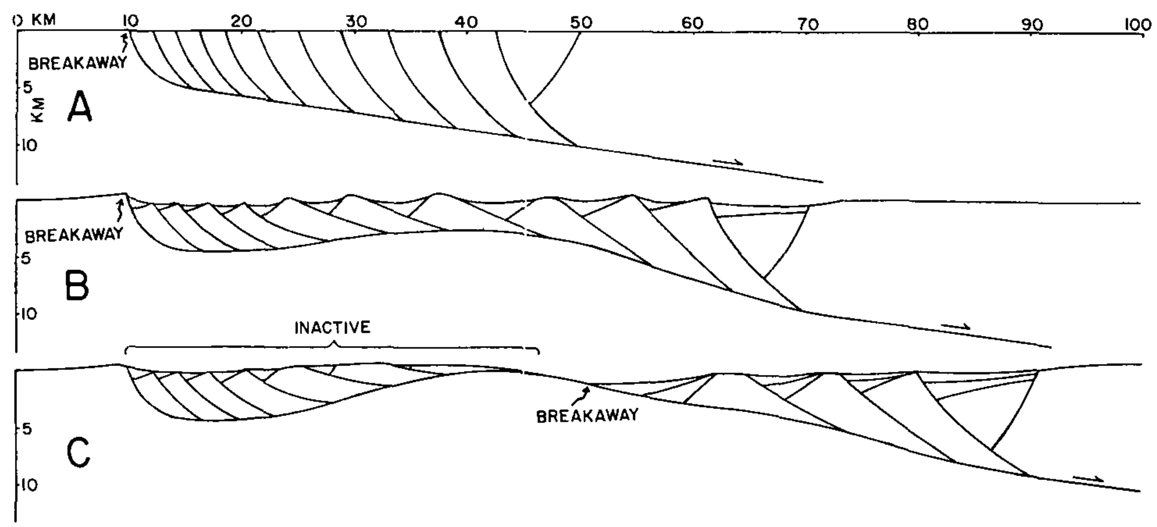

Figure 2. Schematic diagram of warping and uplift of detachment fault. A: Inception of master detachment fault and subsidiary normal faults within upper plate. B: After 20 km of extension an antiformal warp has developed. Shape of warp and amount of uplift are depicted in listric model of Figure 1 (solid line). Antiform is becoming barrier to movement of upper plate from left, upper plate in area of synformal warping is becoming inactive, and one-sided denudation of antiform is about to begin. C: 20 km of one-sided denudation has resulted in further uplift and initial exposure of lower plate to subareal erosion. Shape of basal detachment fault and distribution of extension during one-sided denudation resemble planar detachment of Figure 1 and skewed distribution of extension (dashed line, Fig. 1), resulting in subdued arching of fault surface and amplified uplift in breakaway area.

Spencer, Geology, 1984

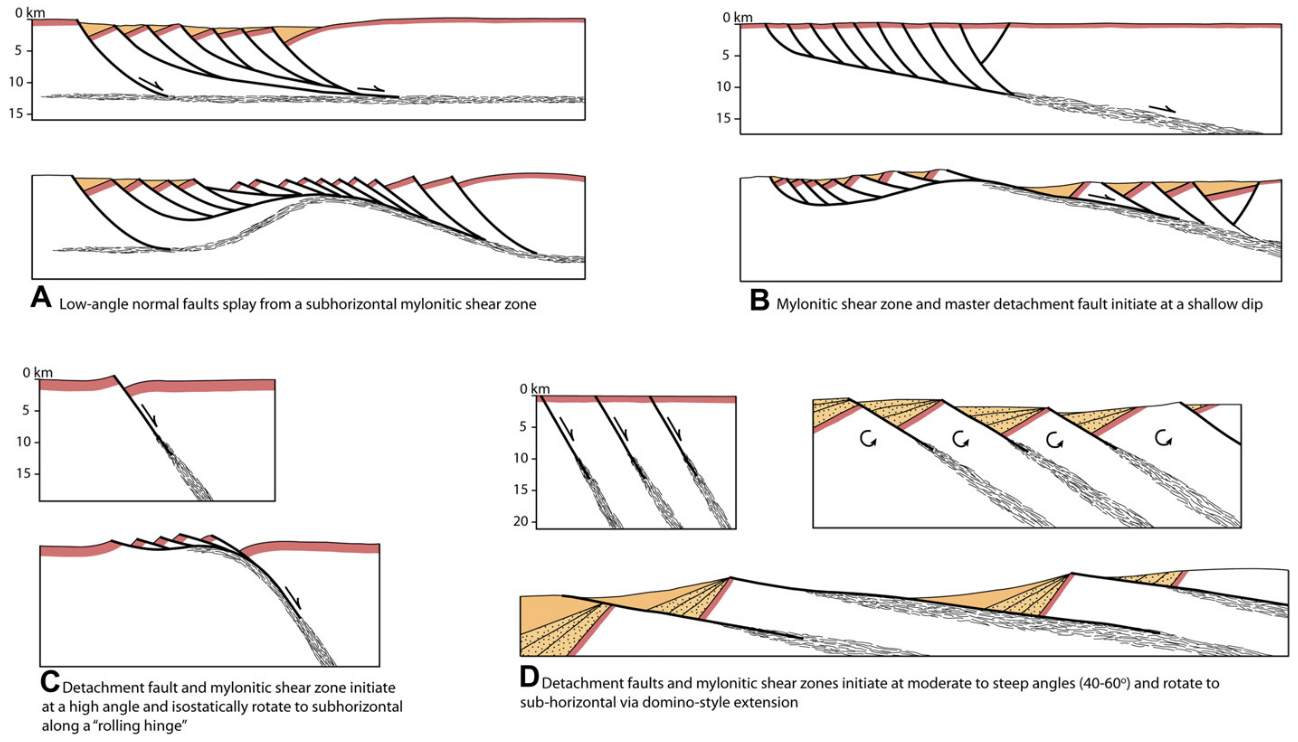

Singleton & Mosher, J Struct Geol, 2012

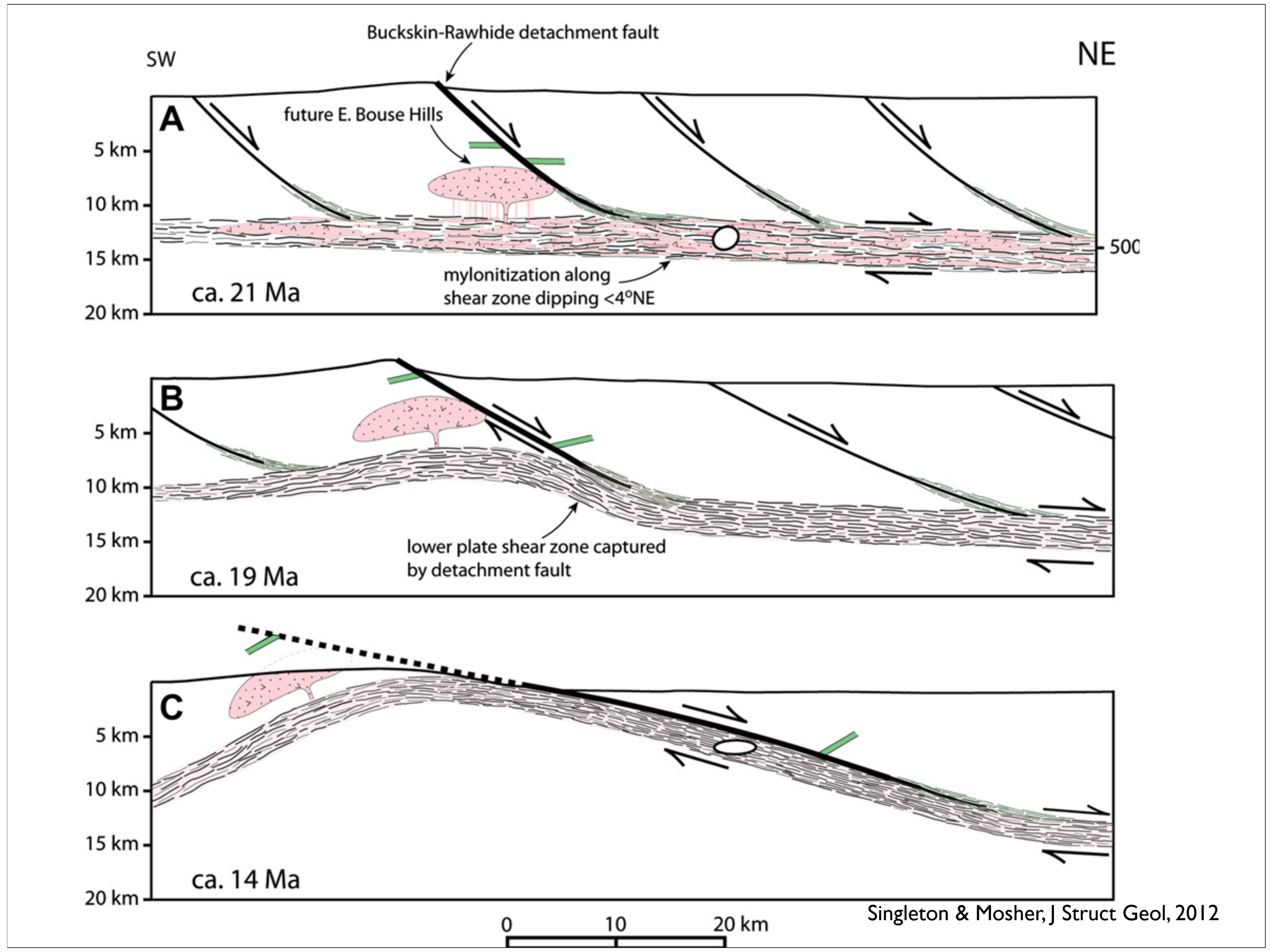

Based on temp est from quartz deformation in mylonites, argue shear zone initiated as a very flat feature but think that the upper plate faults were much steeper.